Electronic Supplementary Information

Data-Driven Prediction of Grain Boundary Segregation and Disordering in High-Entropy Alloys in a 5D Space

Chongze Hu[1, 2, #] and Jian Luo[1, 2, *]

[1]*Department of Nanoengineering;* [2]*Program of Materials Science and Engineering,*
University of California San Diego,
La Jolla, California 92093, USA

*Corresponding author. E-mail: jluo@alum.mit.edu (J.L.)

[#]Current address: Center for Integrated Nanotechnologies, Sandia National Laboratories, Albuquerque, New Mexico 87185, USA

Table of Contents

Supplementary Discussion

Supplementary Discussion 1: Principal component analysis (PCA) of the HEA selection

In this work, we adopted a conventional definition of HEAs: *i.e.*, the composition of each element in $Cr_xMn_yFe_zCo_lNi_m$ HEAs follows the relations: (*i*) $0.05 \leq x\ (y, z, l, m) \leq 0.35$ and (*ii*) $x + y + z + l + m = 1$ (all in atomic fractions). Here, we set the step of the elemental fraction as 0.05, so that there are 1371 possible compositions in total. Among them, we randomly selected 258 subsystems. A principal component analysis (PCA) was carried out to verify the randomness of our selection.

First, the PCA for the all-included case (with 1371 HEA compositions) shows that the first three principal components (PC1-3) can evenly distribute in the entire 3D space; there is no clustering by coloring each data using PC4 values (Fig. S1a). This also suggests that PC1-4 are highly independent variables. Second, the PCA for our selection of the 258 HEAs shows that the selected compositions also occupy in the entire 3D space without clustering (Fig. S1b). Thus, this analysis indicates that our selection is sufficiently random. Furthermore, the PCA scores (Fig. S1c) show that the first four principal components (PC1-4) only vary in a small range from ~30% to ~20% in our selection. This is comparable to the range from ~26% to ~23% for the all-included case. In conclusion, the PCA analysis verified the randomness of our selection of the 258 HEAs. Thus, these 258 HEA compositions were used to perform MC/MD simulations for generating a dataset.

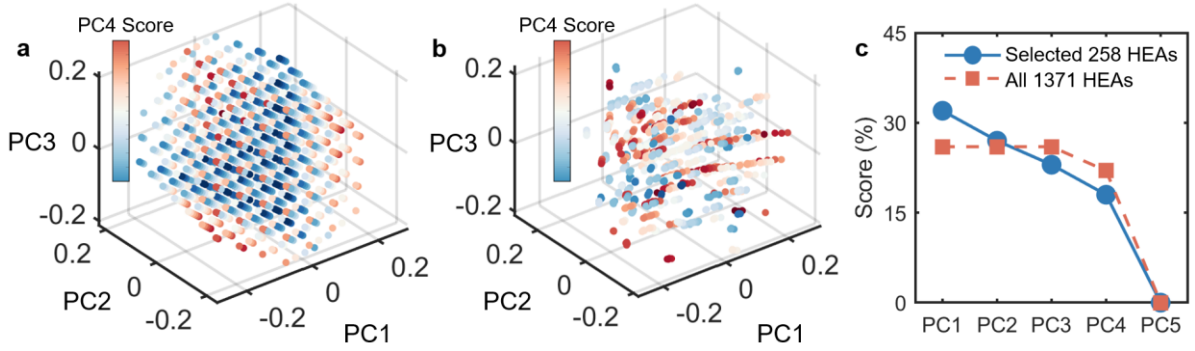

Fig. S1. Principal component analysis (PCA) for the composition distribution of 258 randomly selected HEAs. (**a**) PCA plot of the first three principal components (PC1-3) for all 1371 $Cr_xMn_yFe_zCo_lNi_m$ compositions, where $x + y + z + l + m = 0$, and $0.05 \leq x\ (y, z, l, m) \leq 0.35$. (**b**) PCA plot of PC1-3 for the 258 selected compositions. (**c**) The PCA scores for five principal components of all possible *vs.* selected HEA compositions.

Supplementary Discussion 2: Benchmark and validation of our *NPT* simulations with prior *NVT* simulations and prior experiments

2.1 Comparison of our *NPT* simulations with prior *NVT* simulations

We compare our constant-*NPT* hybrid Monte Carlo and molecular dynamics (hybrid MC/MD) simulations with prior constant-*NVT* Monte Carlo (MC) simulations.[1] We first calculated the GB excess of solute or adsorption (Γ_i , i = Cr, Mn, Fe, Co, and Ni) for the equimolar $Cr_{0.2}Mn_{0.2}Fe_{0.2}Co_{0.2}Ni_{0.2}$ (the Cantor alloy) using a Σ13 twist GB. Fig. S2A shows *NPT*-simulated Γ_i as a function of temperature with the following general trends:

- Γ_{Cr} and Γ_{Mn} are positive (segregation at the GB) and they both decay with temperature.
- Γ_{Fe} and Γ_{Co} are negative (depletion at the GB) and they both increase with temperature.
- Γ_{Ni} is slightly negative and it is almost independent of temperature. These results indicate that Cr and Mn are favorable to segregate, while Fe and Co are unfavorable to segregate, at HEA GBs, which is in a good agreement with prior *NVT*-based MC simulations (Fig. S2(c)).
- Both *NPT* simulations (Fig. S2(b)) and *NVT* simulations (Fig. S2(d)) show that Cr and Mn have low composition in the bulk phase due to strong segregation at the GB, while Fe and Co exhibit high bulk compositions because of strong depletion. Thus, the isobaric *NPT* simulations adopted in this work can successfully reproduce the segregation behavior of the Cantor alloy compared to prior *NVT* MC simulations.
- The GB excesses of solutes (adsorption amounts) calculated in our constant-*NPT* hybrid MC/MD simulations are typically slightly lower than those obtained in prior constant-*NVT* MC simulations. This may be attributed to that our constant-*NPT* hybrid MC/MD simulations allow the GB free volume to relax (while prior constant-*NVT* MC simulations did not). Note that our constant-*NPT* hybrid MC/MD simulations also have more thermal noises in general.

Since our atomistic model of the GB structure contained a limited number of atoms (~11640 atoms) and we fixed the global composition of each element during the MC/MD simulations, the elemental segregation/depletion to GB region will lower/raise the corresponding grain (bulk) composition of each element (at the center of the grain). It is important to note that we always plot

the GB segregation and other GB properties as functions of the actual bulk composition (measured at the center of the grain, instead of the global composition) and our grain size is sufficient large. Thus, the results should be independent of the grain size.

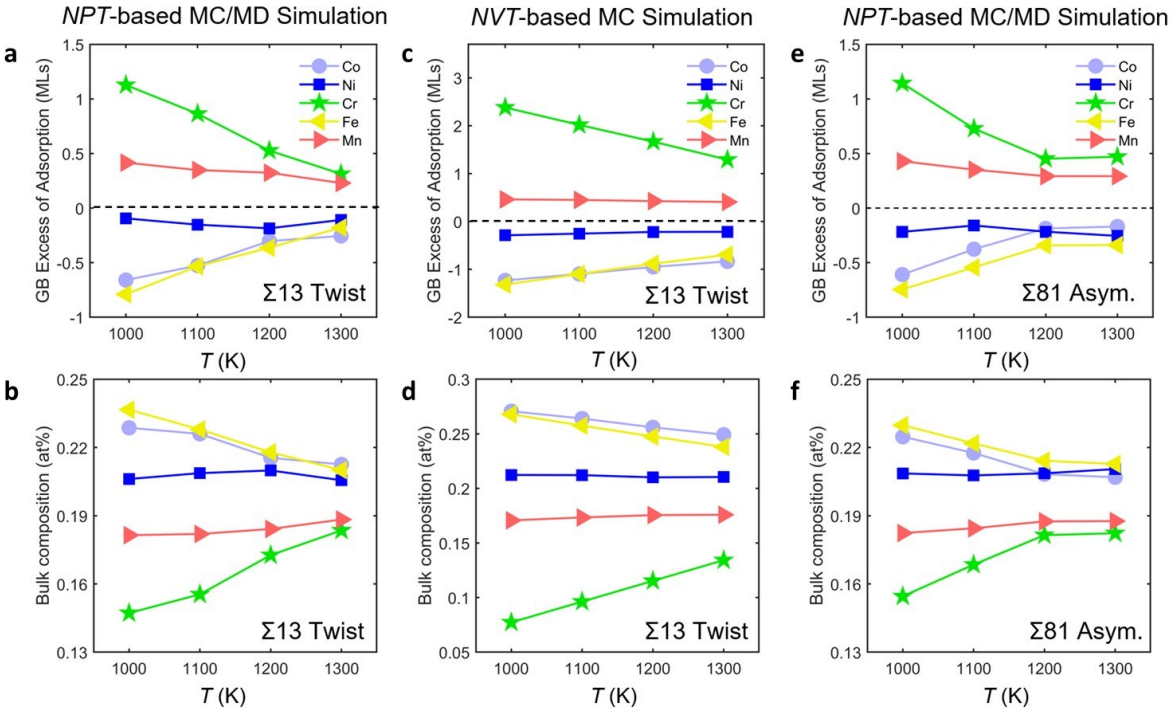

Fig. S2. Benchmark of *NPT*-based hybrid MC/MD simulations *vs*. *NVT*-based MC simulation on the equimolar $Cr_{0.2}Mn_{0.2}Fe_{0.2}Co_{0.2}Ni_{0.2}$. (**a**) The GB excess of segregation of each element and (**b**) the corresponding bulk composition from 1000 K to 1300K calculated by *NPT*-based hybrid MC/MD simulations for a Σ13 twist GB. (**c**) The GB excess of segregation and (**d**) the corresponding bulk composition from 1000 K to 1300K based on prior *NVT* simulations, with data extracted from Ref. [1], for the same Σ13 twist GB. (**e**) The calculated GB excess of segregation and (**f**) the corresponding bulk composition obtained by *NPT*-based hybrid MC/MD simulations for a Σ81 asymmetric GB selected for this study. Since we fixed the global composition of each element during the MC/MD simulations, the elemental segregation (*e.g.*, of Cr and Mn) to GB will lower the bulk composition, while the depletion at GB (*e.g.*, of Fe and Co) will raise the bulk (grain) composition. However, we always plot GB properties as a function of bulk composition.

We note that the Σ13 twist GB (investigated in prior study[1] and benchmarked above) is a symmetric (special) GB while the focus of this study is on asymmetric general GBs of mixed tilt and twist characters. Thus, here we selected one (general) asymmetric mixed twist-tilt Σ81 GB with boundary planes $(1\bar{1}0)//(7\bar{8}7)$ to represent general GBs. The hybrid MC/MD simulations showed that the same relative segregation tendency: $\Gamma_{Cr} > \Gamma_{Mn} > 0 \sim \Gamma_{Ni} > \Gamma_{Fe} \sim \Gamma_{Co}$ (Fig. S2e), which is in the same order as that in the symmetric Σ13 twist GB (Fig. S2a). It is interesting to

note that the GB excesses of adsorption and bulk composition for mixed Σ81 GB exhibit more complex (more non-linear) relation as a function of temperature in Fig. S2(e-f). Since asymmetric Σ81 GB has more disordered GB structure than symmetric Σ13 GB, this suggest that such complex GB segregation behavior may be caused by the GB disordering effect.

2.2 Comparison of our simulations with prior experiments

Second, we compare our simulation results with several **experimental studies of CrMnFeCoNi**. This benchmark analysis between our simulations and prior experiments is summarized as follows:

- Several experiments using the atom probe tomography (APT) technique have shown that the GBs in CrMnFeCoNi HEAs are enriched in Cr, Mn, and Ni, but deficient in Fe and Co.[2, 3] Our *NPT*-based MC/MD simulation results showed the relative tendency of GB segregation as: $\Gamma_{\mathrm{Cr}} > \Gamma_{\mathrm{Mn}} > \Gamma_{\mathrm{Ni}} \sim 0 > \Gamma_{\mathrm{Fe}} \sim \Gamma_{\mathrm{Co}}$ (as shown in Fig. S2(e) above as well as Fig. S2(a-b) in main text), which is consistent with the experimental observations.
- Notably, Li *et al.* observed GB spinodal decomposition that formed Cr-rich and Mn-rich regions.[2] We found that GB disordering (that should be more significant at high temperatures) promoted the co-segregation of Cr and Mn (as shown in Fig. 3 in the main text and elaborated further in Supplementary Discussion 4 and Supplementary Discussion 5), which might separate into Cr-rich and Mn-rich upon cooling with less GB disorder. This offers a reasonable explanation of Li *et al.* observation of GB spinodal decomposition with Cr-rich and Mn-rich regions.[2]

In conclusion, our constant-*NPT* hybrid MC/MD simulation results agree well with prior modeling and experimental studies. Moreover, MC/MD simulation results have also been validated by density functional calculation (DFT) calculations, as shown in Supplementary Discussion 10.

Supplementary Discussion 3: Artificial neural network (ANN) performance and validation of the predicted GB diagrams

To validate ANN prediction, we first compare ANN-predicted *vs.* MC/MD-simulated GB properties. In addition to the parity plot of ANN-predicted *vs.* MC/MD-simulated Γ_{Cr} values as shown in Fig. 2A in the main text, other parity plots of GB properties are shown in Fig. S3. The results show that good linear relations can be achieved for Γ_{Co}, Γ_{Fe}, and Γ_{Mn}, but the predictions for Γ_{Ni} and $\Gamma_{\mathrm{Disorder}}$ have larger errors. Further discussion about RMSEs (Fig. S4) can be found in the main text.

To further validate our ANN model, we use structural similarity index (SSIM) to compare the similarity of ANN-predicted *vs.* MC/MD-simulated binary GB diagrams. For example, Fig. 2(b-c) in the main text show ANN-predicted and MC/MD-simulated GB diagrams of Γ_{Cr} as a function of Mn bulk fraction ($x = X_{\mathrm{Mn}}$) of $Cr_{0.4-x}Mn_xFe_{0.2}Co_{0.2}Ni_{0.2}$, where $0.05 \leq x \leq 0.35$. The SSIM value of 0.88 indicates good similarity (SSIM = 1 means same and 0 means different). In addition, high SSIM values (0.85-0.89) can be achieved for predicting Γ_{Cr} in other nine alloys as shown in Fig. S17. Moreover, by calculating the SSIM values for all binary systems, we plotted the SSIM distribution histograms for all GB properties; Fig. S5 shows that high SSIM of ANN-predicted *vs.* MC/MD-simulated GB adsorption properties for Γ_{Mn}, Γ_{Fe}, and Γ_{Co}, but low SSIM values (~0.63-0.66) for Γ_{Ni} and Γ_{Dis}. This agrees with the prior RMSE analysis and parity plots. Therefore, we conclude that our ANN model is robust to predict GB diagrams of strong segregation (*e.g.*, Cr and Mn) or depletion (*e.g.*, Fe and Co) elements, but the performances for predicting Γ_{Ni} and Γ_{Dis} are slightly less.

In all above cases, the relatively lower performances for predicting Γ_{Ni} and Γ_{Dis}, respectively, can be ascribed to the large relative errors due to small absolute Γ_{Ni} values and relatively large errors in quantifying Γ_{Dis}, respectively. Thus, the same levels of thermal noises will cause more relative errors in predicting these two GB properties.

The ANN-predicted GB diagrams show a merit of machine learning: it can be used as a smoothing function to reduce the large random errors in MC/MD simulations due to thermal noises. This smoothing effect can be demonstrated by comparing MC/MD-simulated *vs.* ANN-predicted Γ_{Cr} curves for ten different alloys at 1000 K in Fig. S6(a).

Furthermore, the ANN model is significantly more efficient than MC/MD simulations to predict GB diagrams with multiple variables.

We have plotted all possible ANN-predicted *vs.* MC/MD-simulated binary GB diagrams in Figs. S17-S22.

In Fig. 2D-I in the main text, we show one example of six GB properties of $Cr_xMn_{0.2}Fe_yCo_{0.2}Ni_z$, where $x + y + z = 0.6$, at 1000 K. Fig. S23 shows another example of ternary GB diagrams of Γ_{Cr} for 10 different alloys at 1000 K.

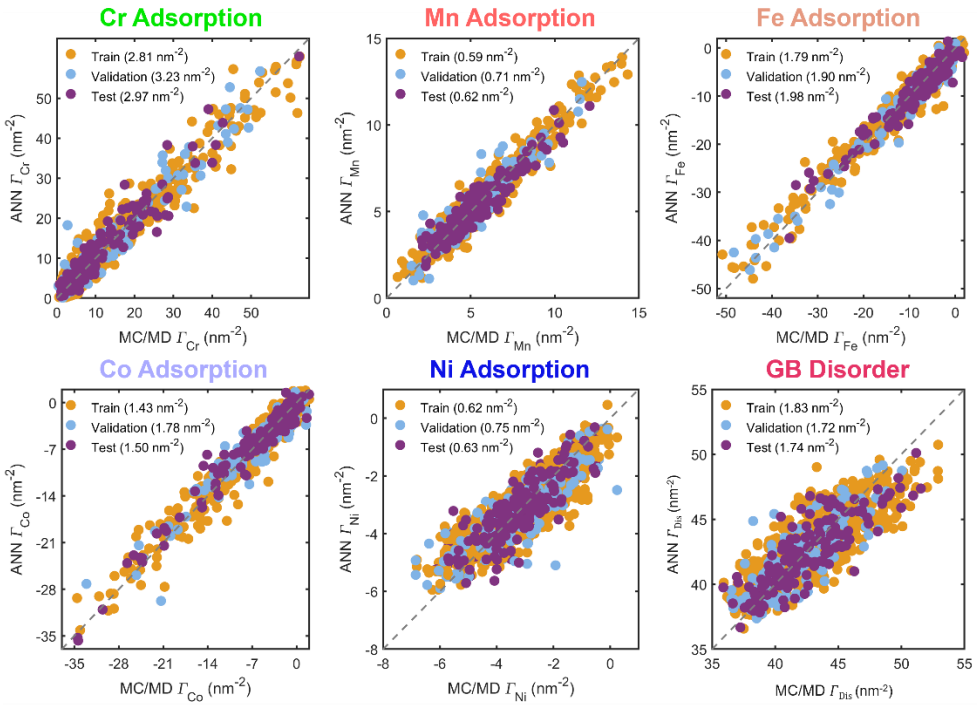

Fig. S3. Performance of ANN model for predicting GB properties in HEAs. Parity plots for ANN-predicted *vs.* MC/MD-simulated GB adsorption amounts (*i.e.*, Γ_{Cr}, Γ_{Mn}, Γ_{Fe}, Γ_{Co}, Γ_{Ni}) and excess disorder (Γ_{Dis}). The root-mean-square errors (RMSE) of training, validation, and test sets are labelled. Notably, the ANN models can always outperform than statistical models for predicting GB properties.

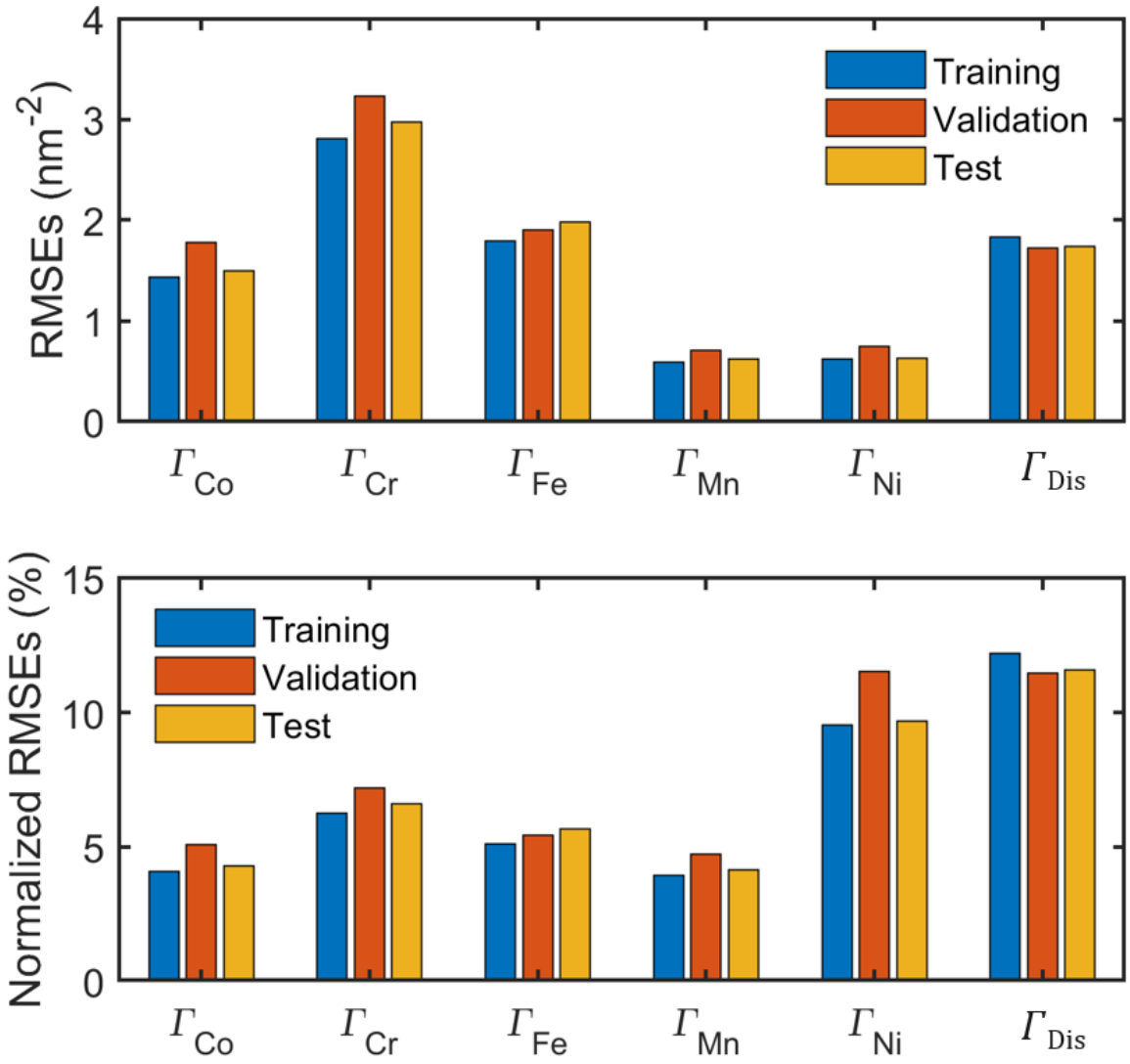

Fig. S4. Root-mean-square errors (RMSEs) of the ANN model. Histograms of RMSEs of the ANN training, evaluation, and test data sets (shown in the upper panel) for six GB properties (*i.e.*, $\Gamma_{Cr}, \Gamma_{Mn}, \Gamma_{Fe}, \Gamma_{Co}, \Gamma_{Ni}$, and Γ_{Dis}). Histograms of normalized RMSEs (divided by maximal values or maximal variation ranges) of the ANN training, evaluation, and test data sets (shown in the bottom panel) for these six GB properties.

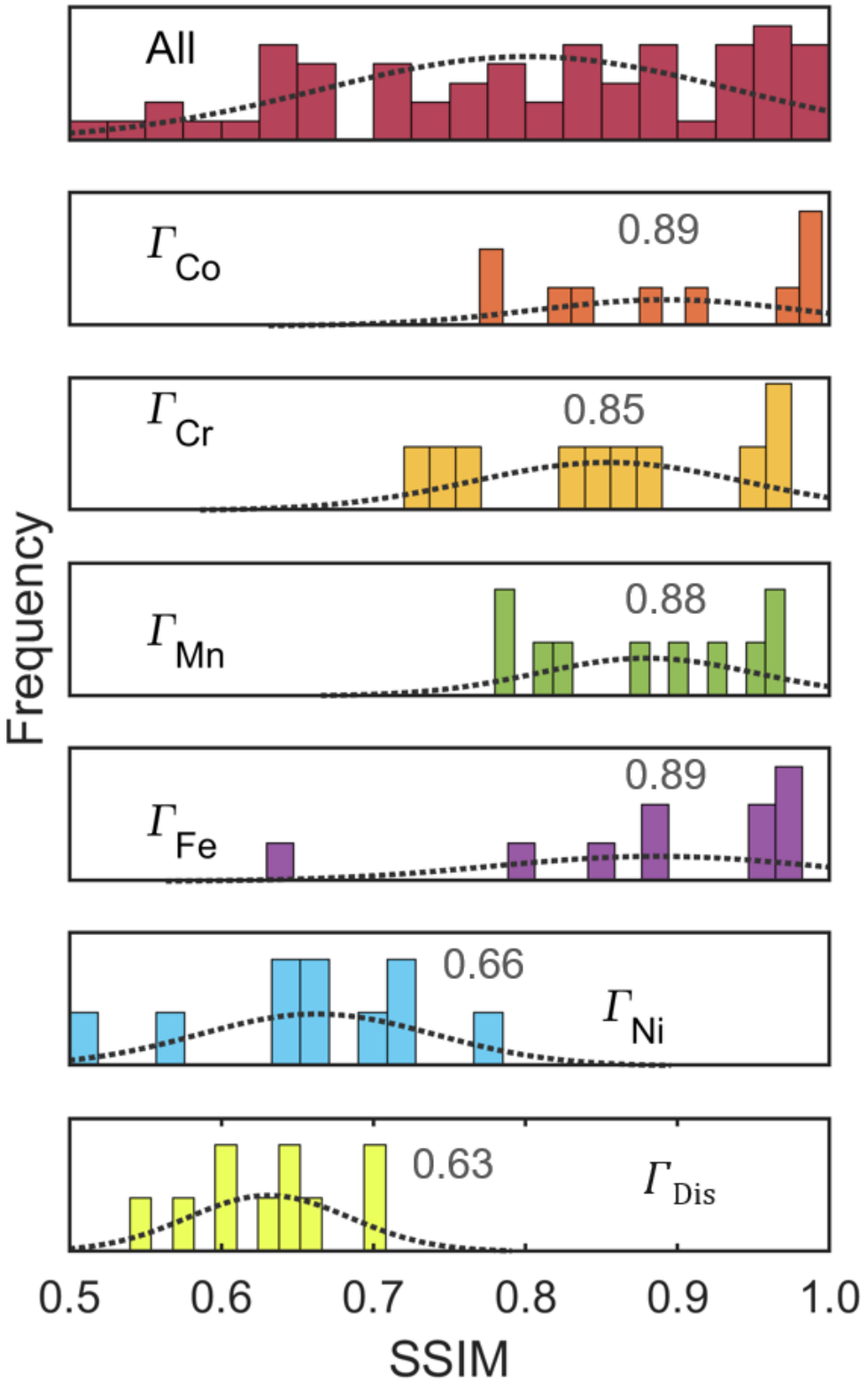

Fig. S5. Histograms of structural similarity index (SSIM) of ANN-predicted *vs*. MC/MD-simulated binary GB diagrams for six GB properties. The detailed SSIM values of each pair of GB diagrams can be found in Fig. S14-S19.

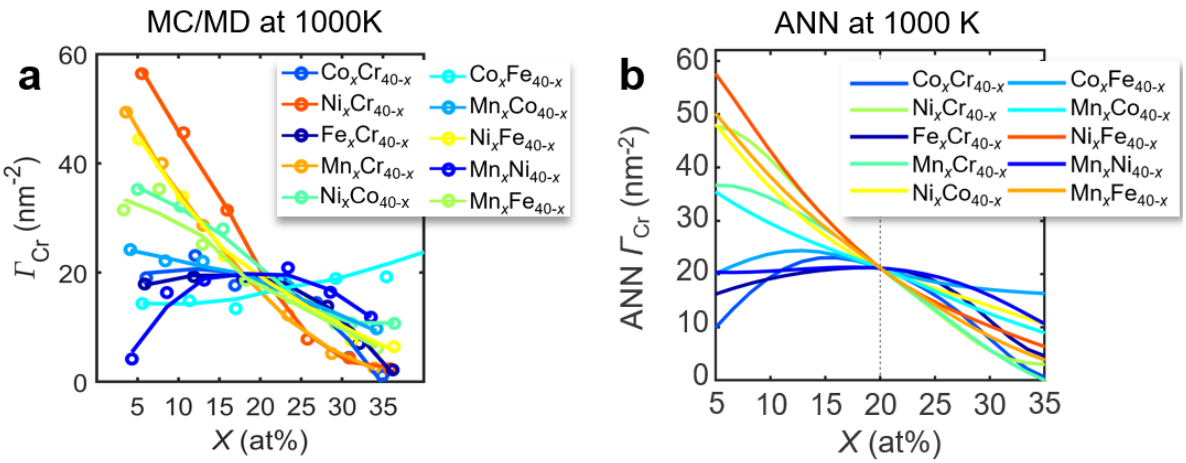

Fig. S6. MC/MD simulation *vs.* ANN prediction for ten alloys. Here, for example, the notation "Co_xCr_{40-x}" represents $Cr_{40-x}Mn_{0.2}Fe_{0.2}Co_xNi_{0.2}$ as a function of the Co bulk fraction x, balanced by Cr. (**a**) MC/MD-simulated Γ_{Cr} curves *vs.* the compositional variable x for 10 different cases at 1000 K. (**b**) ANN-predicted Γ_{Cr} curves for the 10 different cases at 1000 K.

Supplementary Discussion 4: Coupling of the segregation of multiple elements and interfacial disordering

4.1 Couplings among the segregation of multiple elements

In HEAs, several elements can segregate at HEA GBs simultaneously, which may subsequently enhance GB disordering. To further understand the simultaneous segregation of multiple elements, disordering, and their coupling effects, we applied hybrid MC/MD simulations to systematically study GBs in nine different ternary (medium-entropy) to quinary (high-entropy) alloys from 1000 K to 1300 K. We calculated the GB excess of adsorption Γ_i (i = Cr, Mn, Fe, Co, Ni) for each alloy. Fig. S7(a) shows the evolution map of calculated Γ_i from ternary (*e.g.*, FeCoNi) to quinary (*e.g.*, CrMnFeCoNi) alloys at 1000 K. Here, all alloys are equimolar except for the case of $Cr_{0.25}Mn_{0.5}Fe_{0.25}$ because equimolar CrMnFe cannot maintain the FCC structure after energy minimization. We draw a schematic diagram in Fig. S7(b). Several key observations can be summarized as follows:

- In equimolar CrMnFeCoNi, Cr and Mn strongly segregate at GBs (labelled in blue in Fig. S7(b)), but Fe and Co strongly deplete at GBs (labelled in purple in Fig. S7(b)).
- When strong segregation elements (*e.g.*, Cr and Mn) and depletion elements (*e.g.*, Fe and Co) are mixed together in ternary alloys, the overall segregation is weak. For example, FeCoNi and CrMnNi both exhibit weak GB segregation (Fig. S7(a)). This can be explained from that Cr and Mn compete segregation sites in ternary alloys.
- Without Mn, the Cr segregation at GBs is weak in both ternary (*e.g.*, CrFeNi and CrCoFe) and quaternary (*e.g.*, CrFeCoNi) alloys. The Cr depletion at the GB can be ascribed to the agglomeration of Cr inside the grains (see Fig. S7(b) in the main text).
- In quaternary and quinary alloys, the coexistence of Fe and Co atoms may enhance the segregation of both elements. For example, the GB segregation in CrMnFeCo and CrMnFeCoNi are stronger than that in CrMnFeNi.
- Comparing CrMnFeCo and CrMnFeCoNi alloys suggests that Ni atoms can inhibit the overall GB segregation. This can be ascribed to the weak segregation of Ni.
- The co-segregation of Cr and Mn will “push” Fe and Co to bulk phases and result in the depletion of Fe and Co at the GBs. For example, in FeCoNi (without Cr or Mn), both Fe

and Co slightly segregate at the GB, but they do not segregate at CrMnFeNi, CrMnFeCo, and CrMnFeCoNi GBs significantly when Cr and Mn co-segregate at the GBs (Fig. S7(a)).

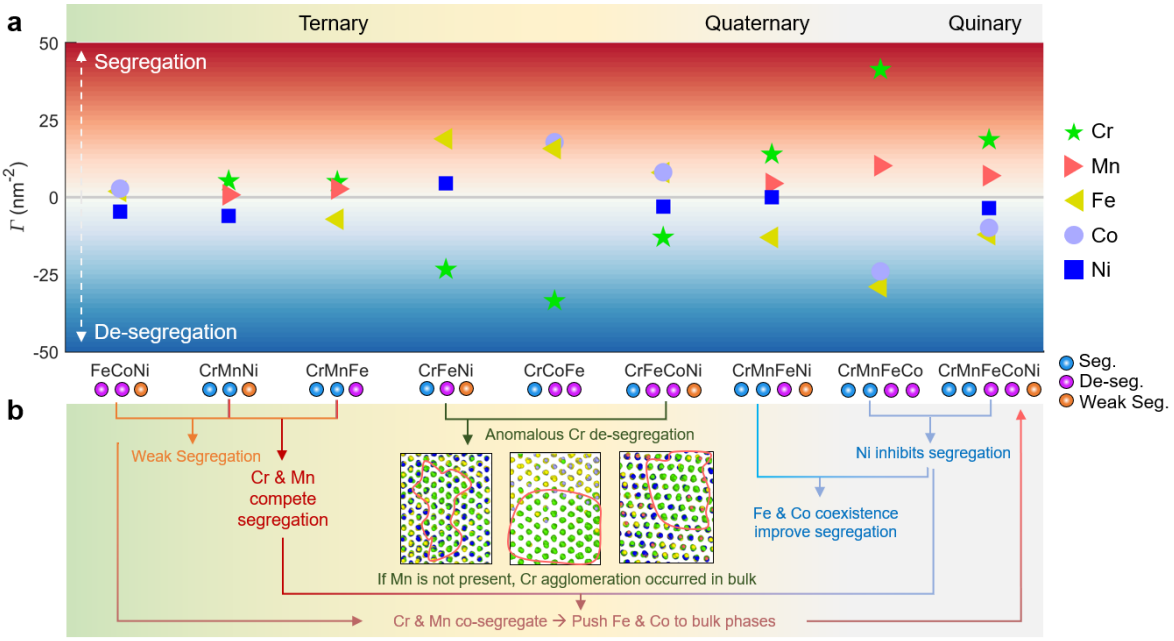

Fig. S7. Segregation of multiple elements at GBs in HEAs. (**a**) The evolution of GB excess of each element at 1000 K from ternary (medium-entropy) to quinary (high-entropy) alloys. All alloys are under equimolar except $Cr_{0.25}Mn_{0.5}Fe_{0.25}$. (**b**) Schematic diagrams of the various interaction effects on GB segregation. The segregation elements (*e.g.*, Cr and Mn) are labelled in blue, while the depletion elements (*e.g.*, Fe and Co) are labelled in purple. The weak segregating (almost neutral) Ni is labelled in orange.

4.2 The effects of interfacial disordering on GB segregation

The GB disordering can be further studied by analyzing the MC/MD-simulated GB structures. First, Fig. S8(a) shows the disorder profile of the nine ternary to quinary alloys at 1000 K, where red color indicates disordered structure (disorder parameter = 1 for a liquid), while the blue color means ordered structure (disorder parameter = 0 for a perfect crystal). It shows that GB disordering tends to increase from ternary to quinary alloys. For example, the Γ_{Dis} values of ternary alloys such as FeCoNi, CrMnNi, and CrMnFe are ~38 to 40 nm^{-2}, but the quaternary CrMnFeCo has a Γ_{Dis} of 50 nm^{-2} and the quinary CrMnFeCoNi has a Γ_{Dis} of 43 nm^{-2} (Fig. S8(a)). This suggests that the interaction of multiple elements at the GBs may prompt interfacial disordering. Second, GBs in alloys containing Mn tend to be more disordered. For example, the Γ_{Dis} is only ~37 nm^{-2} even

in the quaternary CrFeCoNi, which is smaller than the Γ_{Dis} of CrMnFeNi (~41 nm^{-2}) and CrMnFeCo (~50 nm^{-2}), as illustrated in Fig. S8(a). This indicates that Mn may induce GB disordering.

To further analyze the Mn effects on GB structure, we performed polyhedral template matching (PTM) analysis [4] (a more accurate method to quantize structure fraction compared to common neighbor analysis) and plotted the structural fraction of each alloy in Fig. S8(b). It shows that the alloys with Mn atoms always exhibit larger fractions of HCP-like structures. For instance, the CrMnFe contains ~10% HCP-like structures but FeCoNi only has ~5% (Fig. S8(b)). Therefore, the GB disordering induced by Mn may be ascribed to the tendency to form HCP-like structures with Mn at GBs.

In addition, it is interesting to investigate the correlation function between Γ_{Dis} *vs.* Γ_i from ternary to quinary alloys (Fig. S8(c)). First, we generated four different non-equimolar alloys for each combination of elements and performed MC/MD simulations from 1000 K to 1300 K with a step of 1000 K. Then, we computed the correlation coefficients between Γ_{Dis} *vs.* Γ_i based on all data. Fig. S8(c) shows the evolution of Γ_{Dis} *vs.* Γ_i correlation from ternary to quinary alloys, where "1" represents the positive correlation (shown in red), while "-1" means the negative correlation (shown in blue). Here, several key observations can be summarized as follows:

- Mn can induce strong interfacial disordering at HEA GBs. The larger GB disordering can further prompt the co-segregation of Cr and Mn (with depletion of Fe and Co) at HEA GBs.
- GB disorder has weak effect on Ni segregation at GB due to weak depletion.
- The $\Gamma_{\mathrm{Dis.}}$ *vs.* Γ_i correlations are stronger in disordered GBs. For example, the $\Gamma_{\mathrm{Dis.}}$ *vs.* Γ_i correlation in CrMnFe and CrMnFeCo, respectively, is stronger than that in FeCoNi and CrFeCoNi, respectively. This indicates that GB disordering plays an important role on the GB segregation.
- Γ_{Dis} *vs.* Γ_{Cr} has negative correlation relations for ternary alloys, but the correlations become positive for quaternary and quinary alloys.
- The correlation of Γ_{Dis} *vs.* Γ_{Ni}, which can be evident to some extent in ternary alloys, vanishes in quaternary and quinary alloys.

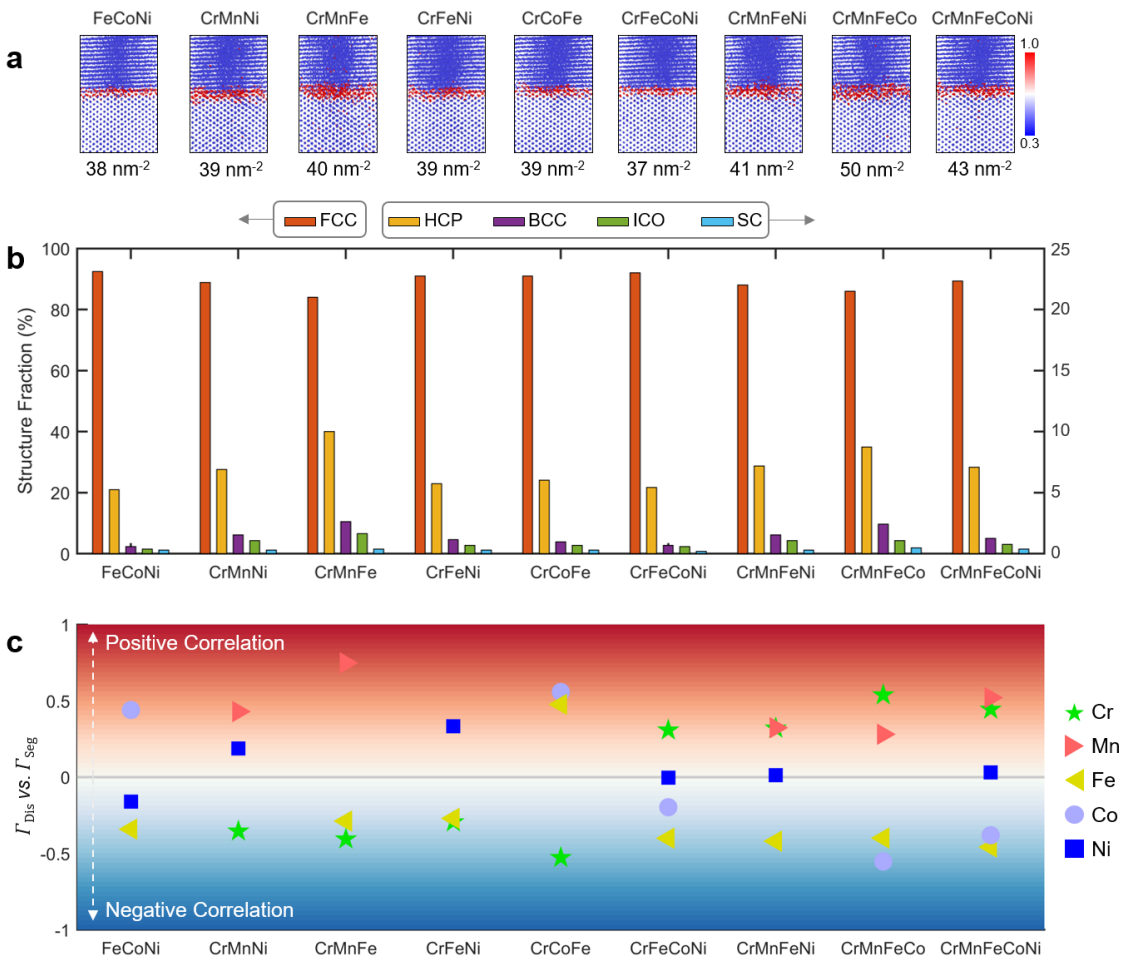

Fig. S8. Effects of GB disordering in HEAs. (**a**) Screenshots of the disorder profiles in MC/MD-simulated GB structures from ternary to quinary alloys at 1000 K. The red color means disordered GBs, and the blue color represents ordered GBs. (**b**) Local structural environment of MC/MD-simulated GB structures at 1000 K from ternary to quinary alloys based on polyhedral template matching (PTM) method. (**c**) The correlation functions of GB excess of adsorption of each element *vs*. GB disorder from ternary to quinary alloys.

Supplementary Discussion 5: Correlation analysis between GB properties

Based on the 1032 MC/MD-simulated data points, we can compute Pearson correlation coefficients (PCCs) between each pair of GB properties (*i.e.*, Γ_{Cr} , Γ_{Mn}, Γ_{Fe}, Γ_{Co}, Γ_{Ni} , Γ_{Dis}, V_{Free}). Fig. 4A in the main text shows the heat map of PCCs. In addition, we can calculate the PCCs between GB properties at different temperatures to understand the temperature effects. Fig. S9(a-d) show the heat map of PCCs from 1000 K to 1300 K. Several findings can be summarized as follows:

- By comparing the PCCs between each pair of five GB adsorption properties ($\Gamma_{\mathrm{Cr}}, \Gamma_{\mathrm{Mn}}, \Gamma_{\mathrm{Fe}}, \Gamma_{\mathrm{Co}}, \Gamma_{\mathrm{Ni}}$), we found weak temperature effects. For example, the correlation coefficients of Γ_{Cr} *vs.* Γ_{Mn} are almost same from 1000 K to 1300 K, which are 0.84, 0.85, 0.84, and 0.77, respectively. Similar observations can be found for other pairs of GB adsorption properties (Fig. S9(a-d)).
- By comparing the correlation between GB disordering (Γ_{Dis}) with any of the GB adsorption properties, we found a strong temperature effect. For example, the PCC of $\Gamma_{\mathrm{Dis}}\ vs.\ \Gamma_{\mathrm{Cr(or\,Mn)}}$ decreases from 0.78 (or 0.73) to 0.35 (or 0.6) when temperature is increased from 1000 K to 1300 K (Fig. S9(e)). The decreasing PCC scores between $\Gamma_{\mathrm{Dis}}\ vs.\ \Gamma_{\mathrm{Cr(or\,Mn)}}$ can be ascribed to the general weak segregation at high temperatures (due to temperature-induced desorption, another thermodynamic effect on segregation beyond GB disorder).
- By comparing the correlation between GB free volume (V_{Free}) with any of the five GB adsorption properties, we again found weak temperature effects. For example, the PCC values of $V_{\mathrm{Free}}\ vs.\ \Gamma_i$ (i = Cr, Mn, Fe, Co, Ni) are very small (virtually zero) and almost remain unchanged when temperature increases (Fig. S9(f)).

In conclusion, the correlation analysis unambiguously indicates the importance of GB disordering on GB segregation in HEAs.

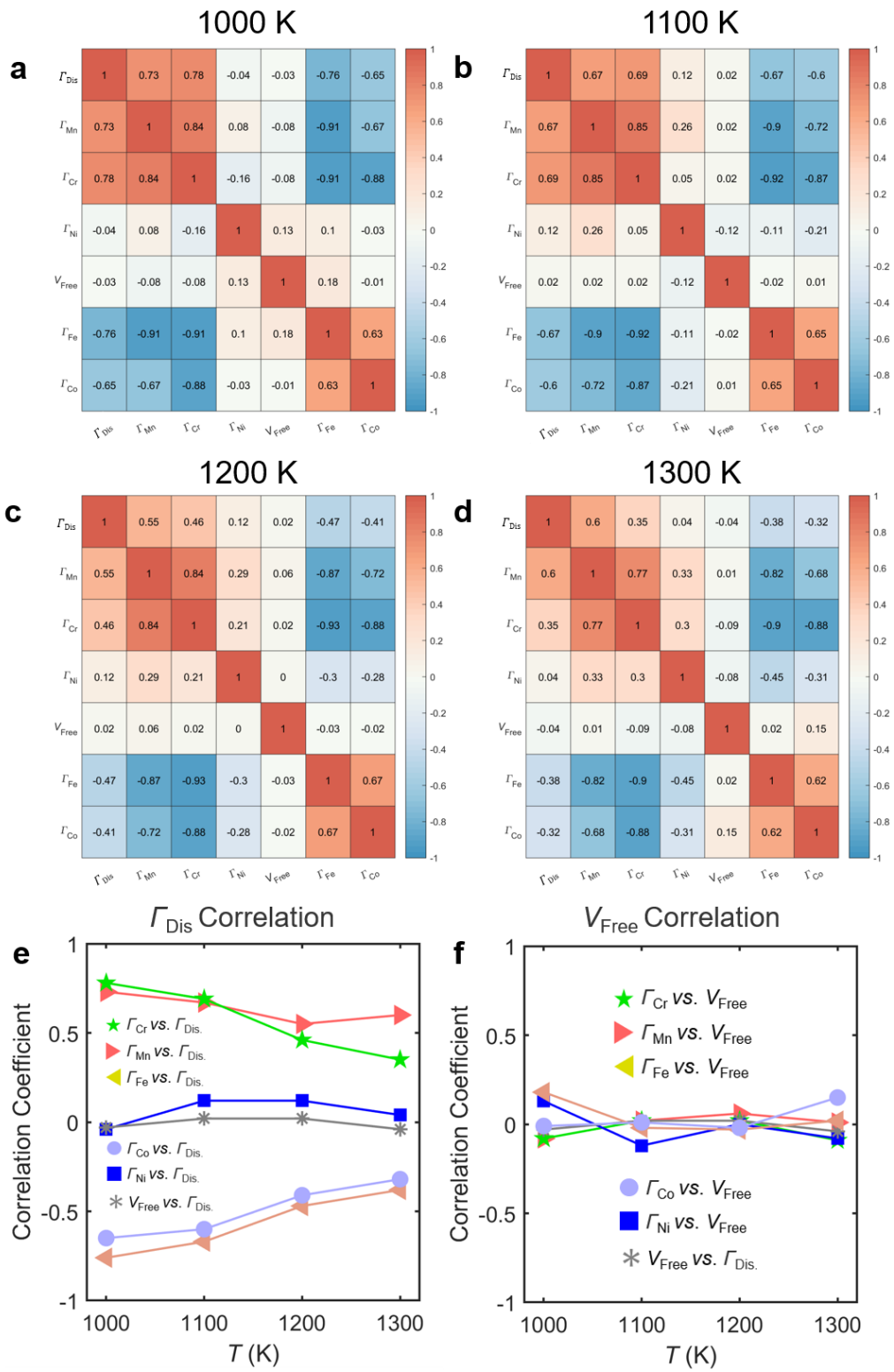

Fig. S9. Correlation between GB properties at different temperatures. (**a-d**) Heat map of correlation coefficients from 1000 to 1300 K. (**e**) The correlation coefficients between Γ_{Dis} and other GB properties at different temperatures. (**f**) The correlation coefficients between Γ_{Dis} and other GB properties at different temperatures.

Supplementary Discussion 6: A physics-informed data-driven model (PIDDM) for predicting GB segregation and disorder in HEAs

Here, we propose a physics-informed data-driven model (PIDDM) to predict the GB excess of solutes and disorder in HEAs. Based on the linear regression analyses shown in Fig. S10(a-e), the adsorption amount (*i.e.*, GB excess of the solute i, where i = Cr, Fe, Co, Ni, Mn), $\Gamma_i(T,X)$, is statistically correlated with the GB excess of disorder, $\Gamma_{Dis}(T,X)$, linearly with the slope $\bar{\alpha}^i_{\mathrm{Dis}}(T)$ at a given temperature T, where $X=\{X_i\}$ is a concise form to note the bulk composition of the HEA. Thus, we statistically have the following linear correlation:

$$\Gamma_i(T,X)-\Gamma_i^0=\bar{\alpha}^i_{\mathrm{Dis}}(T)\cdot[\Gamma_{Dis}(T,X)-\Gamma_{Dis}^0], \tag{S1}$$

where $(\Gamma_i^0\ ,\Gamma_{Dis}^0)$ is the intersection point of all linear regression lines for different temperatures in each panel of Fig. S10(a-e). Here, we use an overbar on $\bar{\alpha}^i_{\mathrm{Dis}}$ to denote that it is a statistically averaged value (but does not represent a simple linear correlation).

It is important to note that we do not suggest a simple linear relation between Γ_{i} and Γ_{Dis} via performing the correlation analysis using Eq. (S1). On the contrary, we know it is not a simple linear relation based the PIDDM discussed below. The scattered data points GB excess of adsorption *vs*. Γ_{Dis} in Fig. S10(a-d) can be ascribed to 258 different compositions $X=\{X_i\}$. However, a hidden statistical correlation does exist after we average over the 258 random $X=\{X_i\}$ values, which are randomly distributed in the 4D compositional space as verified on the PCA in Supplementary Discussion 1.

We can observe in Fig. S10(a-d) that $(\Gamma_i^0\ ,\Gamma_{Dis}^0)$ are virtually independent of temperature and Γ_i^0 is a relatively small number: $\Gamma_i^0 \ll \langle\Gamma_i(T,X)\rangle$. Furthermore, the linear regression analyses shown in Fig. S10(f) suggest:

$$\bar{\alpha}^i_{\mathrm{Dis}}(T)=\ \beta_i\cdot(T-T_{\mathrm{C}}), \tag{S2}$$

where β_i is slope of the linear regression line in Fig. S10(f). Here, $T_{\mathrm{C}}\approx 1388\pm 51$ K (based on the fitting results shown in Table S2) is a critical temperature shown in Fig. S10(f) (and Fig. 4D in the main text). At $T=T_{\mathrm{C}}$, $\Gamma_i(T_C,X)=\Gamma_i^0\sim 0$ (see Fig. S10(a-d)), so this critical temperature is the so-called "compensation" temperature of adsorption/segregation [5], the physical meaning and origin of which will be discussed further in Supplementary Discussion 12.

Combining the linear regression analyses following Eqs. (S1) and (S2), we further propose:

$$\Gamma_i(T,X) = \beta_i \cdot (T - T_{\mathrm{C}}) \cdot [\Gamma_{Dis}(T,X) - \Gamma^0_{\mathrm{Dis}}] + \Gamma^0_i(X). \quad \text{(S3)}$$

Here, we can assume $\Gamma^0_{Dis} = \Gamma^{\min}_{\mathrm{Dis}}$ (or the minimum among all possible HEAs compositions), which are approximately held based on Fig. S10(a-d), except for the case of Ni, where there are too much noises due to the small values of Γ_{Ni}. In Eq. (S1) and Fig. S10(a-d), Γ^0_i is a fitted constant independent of *X*. In Eq. (S3), we further generalize Eq. (S1) to allow this constant Γ^0_i to be a function of *X* to enable more accurate fitting, where we have $\langle \Gamma^0_i(X) \rangle \sim \Gamma^0_i$. Here, we may adopt a linear expression as a first-order approximation:

$$\Gamma^0_i(X) = \sum_j \left(\kappa^{\mathrm{Seg}}_{i,j} \cdot X_j \right) \quad \text{(S4)}$$

where $\kappa^{\mathrm{Seg}}_{i,j}$ is a coupling coefficient for GB segregation. Thus, we have:

$$\Gamma_i(T,X) = \beta_i \cdot (T - T_{\mathrm{c}}) \cdot [\Gamma_{Dis}(T,X) - \Gamma^0_{\mathrm{Dis}}] + \sum_j \left(\kappa^{\mathrm{Seg}}_{i,j} \cdot X_j \right). \quad \text{(S5)}$$

Since GB disorder should increase with temperature, we further propose the following relation:

$$\Gamma_{Dis}(T,X) = \Gamma_{Dis,0}(X) \cdot \exp\left(-\frac{E^{Dis}_A}{k_{\mathrm{B}} T} \right). \quad \text{(S6)}$$

where E^{Dis}_A is the activation energy of disordering, k_{B} is the Boltzmann constant. We again adopt a linear expression as a first-order approximation for the temperature-independent pre-factor:

$$\Gamma_{Dis,0}(X) = \sum_i \left(\kappa^{\mathrm{Dis}}_i \cdot X_i \right) \quad \text{(S7)}$$

Next, we can use all hybrid MC/MD-simulated data points to fit Eq. (S6) and Eq. (S7). The results are shown in Table S1 below.

Table S1. Fitted coefficients for Eq. (S6) and Eq. (S7). The E^{Dis}_A is the activation energy and κ^{Dis}_i is the compositional coefficients for GB disorder, where i = Cr, Mn, Fe, Co, Ni. The root-mean-square errors (RMSEs) of the PIDDM and the ANN model are also tabulated.

$\kappa^{\mathrm{Dis}}_{\mathrm{Cr}}$	$\kappa^{\mathrm{Dis}}_{\mathrm{Mn}}$	$\kappa^{\mathrm{Dis}}_{\mathrm{Fe}}$ (nm^{-2})	$\kappa^{\mathrm{Dis}}_{\mathrm{Co}}$	$\kappa^{\mathrm{Dis}}_{\mathrm{Ni}}$	E^{Dis}_A (meV)	**PIDDM RMSE** (nm^{-2})	**ANN RMSE** (nm^{-2})
52	49	46	44	23	-15.4	2.4	1.8

By analyzing the fitted coefficients listed in Table S1, we made several observations:

- Cr and Mn have largest compositional coupling coefficients with GB disorder ($\kappa_{\mathrm{Cr}}^{\mathrm{Dis}}$ and $\kappa_{\mathrm{Mn}}^{\mathrm{Dis}}$), thereby suggesting that these two elements are most likely to induce GB disordering.
- Fe and Co have median coupling coefficients $\kappa_{\mathrm{Fe}}^{\mathrm{Dis}}$ and $\kappa_{\mathrm{Co}}^{\mathrm{Dis}}$ among five elements
- Ni has the smallest $\kappa_{\mathrm{Ni}}^{\mathrm{Dis}}$.

Here, $E_{\mathrm{A}}^{\mathrm{Dis}}$ is an activation energy in an Arrhenius fitting of the dependence of GB disorder Γ_{Dis} on temperature.

Combining Eqs. (S5-S7), we have:

$$\Gamma_i(T,X) = \beta_i \cdot (T - T_{\mathrm{C}}) \cdot \left[\sum_i(\kappa_i^{\mathrm{Dis}} \cdot X_i) \exp\left(-\frac{E_A^{Dis}}{k_{\mathrm{B}}T}\right) - \Gamma_{\mathrm{Dis}}^0\right] + \sum_j\left(\kappa_{i,j}^{\mathrm{Seg}} \cdot X_j\right). \quad \text{(S8)}$$

Then, we can use our hybrid MC/MD-simulated data points to fit Eq. (S8) and the fitted parameters are shown in Table S2.

Notably, the predicted Γ_{Dis} values based on the PIDDM or Eq. (S8) correlate well with MC/MD-simulated results (Fig. S11). The relatively small RMSEs of the surrogate PIDDM shown in Table S2, which are about twice of the ANN model but still satisfactorily good, further indicate the good predictivity of Eq. (S8) or the surrogate PIDDM.

Table S2. Fitted coefficients of the PIDDM using 1032 hybrid MC/MD data points based on Eq. (S8). The root-mean-square errors (RMSEs) of the PIDDM *vs.* ANN predictions are also tabulated. The RMSEs of ANN models are averaged values of training, evaluation, and test sets.

i =	T_{C} (K)	β_i (K^{-1})	$\kappa_{i,\mathrm{Cr}}^{\mathrm{Seg}}$	$\kappa_{i,\mathrm{Mn}}^{\mathrm{Seg}}$	$\kappa_{i,\mathrm{Fe}}^{\mathrm{Seg}}$	$\kappa_{i,\mathrm{Co}}^{\mathrm{Seg}}$	$\kappa_{i,\mathrm{Ni}}^{\mathrm{Seg}}$	PIDDM Prediction RMSE (nm^{-2})	ANN Prediction RMSE (nm^{-2})
			($\mathrm{atom/nm}^2$)						
Cr	1347	-0.0109	32	-47	13	1	-17	7.4	3.0
Mn	1464	-0.0014	1	-5	8	3	1	1.2	0.6
Fe	1370	+0.0075	-13	26	-26	14	14	5.3	1.9
Co	1371	+0.0046	-15	27	4	-17	12	3.8	1.6
Ni	/	~0	-6.4	-3.7	1.2	-0.5	-7.1	0.88	0.7

By analyzing the fitted coefficients listed in Table S2, several interesting observations have been made:

- The fitted critical (compensation) temperature T_{C} are almost the same for all elements (with a moderate difference for Mn with a small slope; it is difficult to determine T_{C} accurately for Ni with a nearly zero slope).
- A large positive $\bar{\alpha}^{i}_{\mathrm{Dis}}$ value, which indicates positive correlation between GB disordering and segregation, is coincident with the strong segregation of *i*. In contrast, a significant negative $\bar{\alpha}^{i}_{\mathrm{Dis}}$ value, which indicates a negative correlation relation between GB disordering and segregation, is coincident with the depletion of *i* at the GB.
- The negative $\kappa^{\mathrm{Seg}}_{\mathrm{Cr,Mn}}$ and $\kappa^{\mathrm{Seg}}_{\mathrm{Cr,Ni}}$ imply that the Cr segregation inhibits the segregation of Mn and Ni. In addition, positive $\kappa^{\mathrm{Seg}}_{\mathrm{Cr,Fe}}$ and $\kappa^{\mathrm{Seg}}_{\mathrm{Cr,Co}}$ indicate that Fe and Co promote the Cr segregation. These predictions agree with our simulation results and the prior analysis.
- The fitted coefficients for Ni are small, which can be ascribed to the weak Ni segregation.
- The two largest fitted $\kappa^{\mathrm{Dis}}_{i}$ values are for Cr and Mn, which strongly promote GB disordering. Prior MC/MD simulations suggest that Mn can induce GB disordering and that GB disordering can promote the Cr co-segregation, which again agree well with these correlation analyses.
- Among all fitted $\kappa^{\mathrm{Dis}}_{i}$ values, $\kappa^{\mathrm{Dis}}_{\mathrm{Ni}}$ is the smallest, which indicates Ni has a weak effect on promote GB disordering. This is in an agreement with the prior correlation analysis that Ni has a weak correlation with GB disordering.

In addition, we have summarized all the regression coefficients in a table below the caption of Fig. S10.

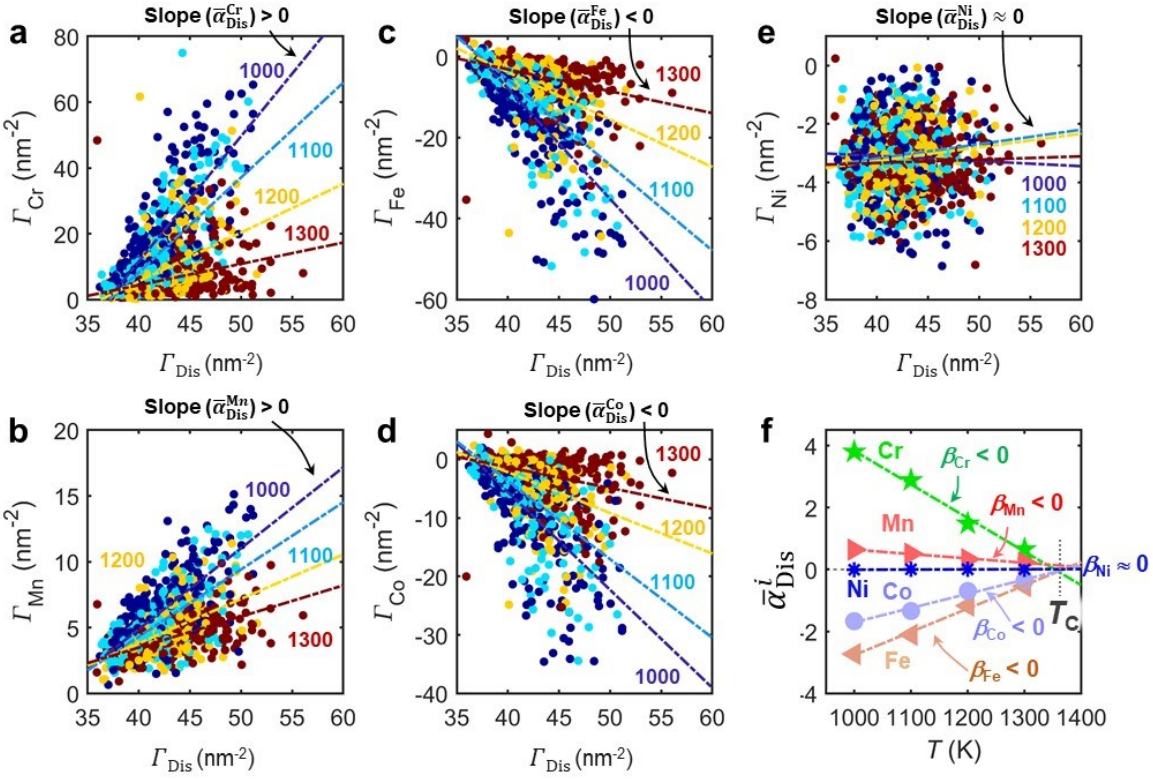

Fig. S10. The relations between GB excess of solutes (adsorption) and disorder. (**a-e**) The relations between Γ_i *vs*. Γ_{Dis} (i = Cr, Mn, Fe, Co, Ni) from 1000 K to 1300 K. The dashed lines represent regression trend lines of $\bar{\Gamma}_i$ *vs*. $\bar{\Gamma}_{\mathrm{Dis}}$ at four different temperature and the slopes of these lines were labelled as $\bar{\alpha}^{i}_{\mathrm{Dis}}$. Here, $\bar{\Gamma}_i$ and $\bar{\Gamma}_{\mathrm{Dis}}$ are the average GB excess of solutes and GB disorder calculated from 258 different HEAs. The regression coefficients ($\bar{\alpha}^{\mathrm{Cr}}_{\mathrm{Dis}}$ and b) of each set of data was fitted from all 1032 MC/MD-simulated data points using the equation $y = \bar{\alpha}^{\mathrm{Cr}}_{\mathrm{Dis}} \cdot \Gamma_{\mathrm{Dis}} + b$. We have summarized all coefficients in the table below. (**f**) Plot of $\bar{\alpha}^{i}_{\mathrm{Dis}}$ *vs*. temperature for five elements. By extending the trendlines of $\bar{\alpha}^{i}_{\mathrm{Dis}}$ *vs*. temperature for five elements, all the lines cross over nearly at same point on x axis. Here, we denoted corresponding temperature as a compensation temperature T_{C}. The slope of $\bar{\alpha}^{i}_{\mathrm{Dis}}$ *vs*. temperature trendlines were labelled as β_i.

T (K)	$\bar{\alpha}^{\mathrm{Cr}}_{\mathrm{Dis}}$	b	$\bar{\alpha}^{\mathrm{Mn}}_{\mathrm{Dis}}$	b	$\bar{\alpha}^{\mathrm{Fe}}_{\mathrm{Dis}}$	b	$\bar{\alpha}^{\mathrm{Co}}_{\mathrm{Dis}}$	b	$\bar{\alpha}^{\mathrm{Ni}}_{\mathrm{Dis}}$	b
1000	3.80	-140.43	0.61	-19.69	-2.73	101.40	-1.67	61.38	-0.02	-2.40
1100	2.88	-106.98	0.51	-16.13	-2.11	78.68	-1.34	50.01	0.05	-5.17
1200	1.48	-53.79	0.34	-9.69	-1.17	43.00	-0.70	25.61	0.05	-5.13
1300	0.65	-21.50	0.24	-5.96	-0.54	18.42	-0.35	12.82	0.01	-3.78

Then, we can use our hybrid MC/MD-simulated data points to fit Eq. (S8) and the fitted parameters are shown in Table S2. Notably, the predicted Γ_{Dis} values based on the PIDDM or Eq. (S8) correlate well with MC/MD-simulated results (Fig. S11). The relatively small RMSEs of the PIDDM, shown in Table S2, which are about twice of the ANN model but still satisfactorily good, further indicate the good predictivity of Eq. (S8) or the PIDDM.

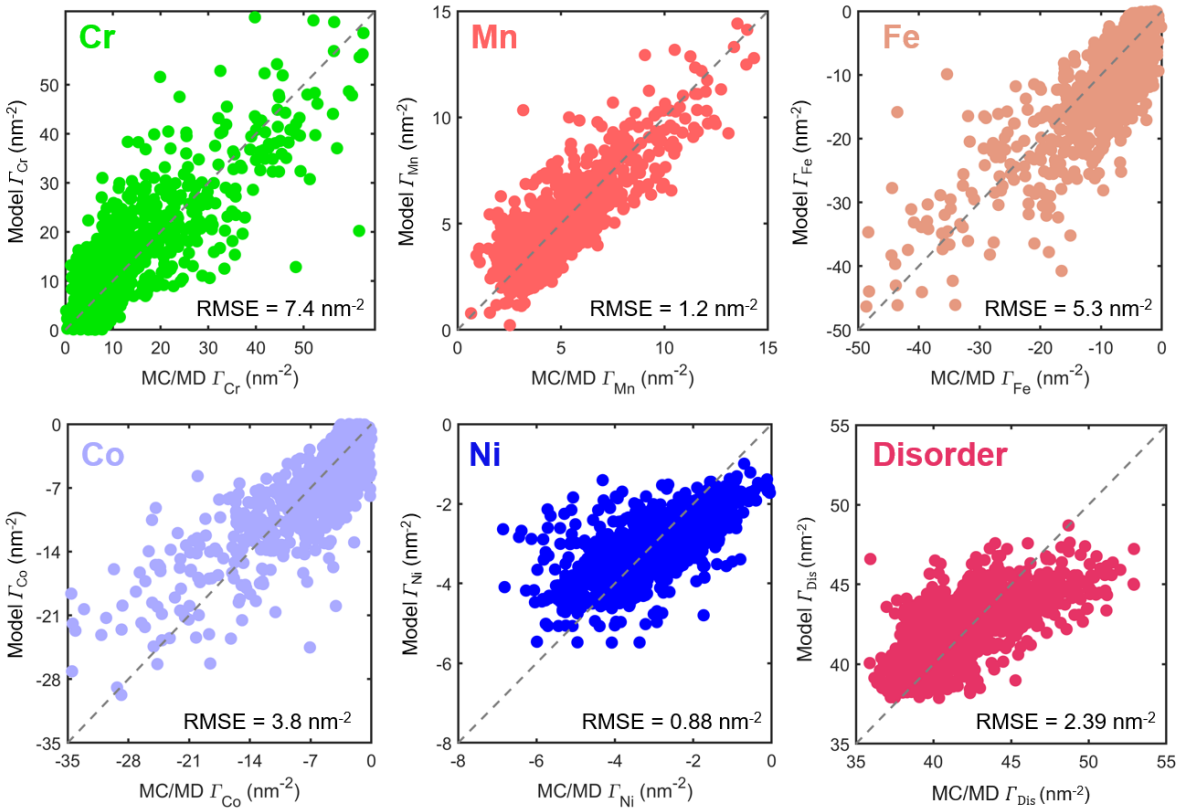

Fig. S11. Performance of our PIDDM for predicting GB properties in HEAs. Parity plots for PIDDM-predicted GB adsorption properties (*i.e.*, Γ_{Cr}, Γ_{Mn}, Γ_{Fe}, Γ_{Co}, Γ_{Ni}) and GB excess of disorder (Γ_{Dis}) *vs.* MC/MD simulations. The root-mean-square errors (RMSEs) between PIDDM predictions and MC/MD simulations are labelled on the bottom right of each plot.

Supplementary Discussion 7: Classical thermodynamic models *vs*. MC/MD simulations of HEAs

The Fowler-Guggenheim isotherm is used for describing GB segregation in binary alloys:[6]

$$\frac{X^{\mathrm{GB}}}{1-X^{\mathrm{GB}}} = \frac{X^{\mathrm{Bulk}}}{1-X^{\mathrm{Bulk}}} exp(-\frac{\Delta H_0^{\mathrm{Seg}} + \omega z X^{\mathrm{GB}}}{k_{\mathrm{B}} T}), \quad \text{(S9)}$$

where ΔH_{Seg}^{o} is intrinsic segregation enthalpy (noting negative ΔH_{Seg}^{o} for preferred segregation), ω is adsorbate-adsorbate interaction parameter, z is coordination number. Wynblatt and Ku [7] further proposed a model to include both chemical and elastic contribution by assuming:

$$\Delta H^{\mathrm{Seg}} = (\gamma_{\mathrm{B}} - \gamma_{\mathrm{A}})\sigma + \omega_{\mathrm{AB}} \left[z^{l} \left(X^{\mathrm{Bulk}} - X^{\mathrm{GB}} \right) + z^{v} \left(X^{\mathrm{Bulk}} - \frac{1}{2} \right) \right] - \Delta E_{\mathrm{el}}, \quad \text{(S10)}$$

where $\gamma_{\mathrm{B(A)}}$ is the surface energy of B (and A) in an A-B alloy (where B is taken as the solute), σ is the area per mole at the interface (for one monolayer), and ω_{AB} is the regular-solution parameter. Here, z^{l} and z^{v} are the numbers of in-plane ("lateral") and (half of) the out-of-plane ("vertical") bonds, respectively. Thus, the total coordination number is given by: $z = z^{l} + 2z^{v}$ (z = 12 for FCC). The elastic strain energy, ΔE_{el}, can be calculated according to the continuum linear elastic formalism originally proposed by Friedel [8]:

$$\Delta E_{\mathrm{el}} = \frac{24\pi K_{\mathrm{B}} G_{\mathrm{A}} r_{\mathrm{B}} (r_{\mathrm{A}} - r_{\mathrm{B}})^2}{3K_{\mathrm{B}} r_{\mathrm{B}} + 4G_{\mathrm{A}} r_{\mathrm{A}}}, \quad \text{(S11)}$$

where K_{B} is the bulk modulus of the solute, G_{A} is the shear modulus of solvent, r_{B} and r_{A} are the atomic radii of the pure solute and solvent atoms. The computed surface energies and atomic radii can be found in Ref. [1]. The interaction parameter, ω_{AB}, can be obtained from mixing enthalpy: $\Delta H_{\mathrm{AB}}^{\mathrm{Mix}} = z \cdot \omega_{\mathrm{AB}}$.[9] For convenience, we have tabulated all binary $\Delta H_{\mathrm{AB}}^{\mathrm{Mix}}$ values for the CrMnFeCoNi system in Table S3 according to Ref. 10.

Here, we calculate the Cr segregation in the Mn, Fe, Co, and Ni based binary alloys to compare with the Cr segregation in HEAs. Fig. 5A in the main text shows the calculated GB fraction (*i.e.* the excess in a monolayer adsorption model) of Cr as a function of the Cr bulk fraction ($x = X_{Cr}^{\mathrm{Bulk}}$) in four binary alloys at 1000 K. The following order of Cr segregation tendency is observed in these four alloys: Fe > Co > Ni > Mn, which is consistent with the calculated segregation enthalpies ($\Delta H_{\mathrm{A,B}}^{\mathrm{Seg}}$, where A is the solute/segregant) listed in Table S3:[10] $\left(-\Delta H_{\mathrm{Cr,Fe}}^{\mathrm{Seg}}\right)$ (3.7 kJ/mol) >

$\left(-H_{\mathrm{Cr,Co}}^{\mathrm{Seg}}\right)$ (2.7 kJ /mol) > $\left(-H_{\mathrm{Cr,Ni}}^{\mathrm{Seg}}\right)$ (-0.7 kJ /mol) > $\left(-H_{\mathrm{Cr,Mn}}^{\mathrm{Seg}}\right)$ (-11.6 kJ /mol). In our definition (sign convention), a negative $\Delta H_{i,j}^{\mathrm{Seg}}$ indicates a preference for segregation, which is the opposite of the sign convention used in the prior model (*i.e.*, a positive segregation enthalpy for segregation).[10] Thus, we use the values of $\left(-\Delta H_{i,j}^{\mathrm{Seg}}\right)$ in discussion, where larger positive $\left(-\Delta H_{i,j}^{\mathrm{Seg}}\right)$ indicates stronger segregation tendency.

To compare simulated GB segregation in HEAs with the GB segregation in binary alloys predicted by the Wynblatt-Ku model,[7] we select four HEAs: $Cr_xMn_{0.4-x}Fe_{0.2}Co_{0.2}Ni_{0.2}$, $Cr_xFe_{0.4-x}Mn_{0.2}Co_{0.2}Ni_{0.2}$, $Cr_xCo_{0.4-x}Fe_{0.2}Mn_{0.2}Ni_{0.2}$, and $Cr_xNi_{0.4-x}Fe_{0.2}Co_{0.2}Mn_{0.2}$ $(0.05 \leq x \leq 0.35)$. We plotted MC/MD-simulated Γ_{Cr} as a function of $x = X_{Cr}^{Bulk}$ in Fig. 5D in the main text.

The MC/MD simulations show different (and more complex) trends of Γ_{Cr} *vs.* x in the four HEAs in comparison with the corresponding benchmark binary alloys predicted by the Wynblatt-Ku model (as shown in Fig. 5D *vs.* 5C in the main text). On the one hand, Γ_{Cr} increases monotonically with increasing x in Cr_xFe_{1-x} and Cr_xCo_{1-x}, which represent two binary alloys with strongest Cr segregation. On the other hand, Γ_{Cr} increases with increasing x initially (for $x < 0.2$) but levels off (for $0.2 < x \leq 0.35$) for $Cr_xFe_{0.4-x}Mn_{0.2}Co_{0.2}Ni_{0.2}$ and $Cr_xCo_{0.4-x}Fe_{0.2}Mn_{0.2}Ni_{0.2}$, with significantly lower Γ_{Cr} levels than those in $Cr_xMn_{0.4-x}Fe_{0.2}Co_{0.2}Ni_{0.2}$ and $Cr_xNi_{0.4-x}Fe_{0.2}Co_{0.2}Mn_{0.2}$ $(0.2 \leq x \leq 0.35)$. Moreover, the MC/MD simulation show that Γ_{Cr} in $Cr_{0.35}Mn_{0.2}Fe_{0.05}Co_{0.2}Ni_{0.2}$ can reach ~1.2 monolayer (ML) at T = 1000 K (Fig. 5D), which is significantly larger than ~0.6 ML in $Cr_{0.35}Fe_{0.65}$ (at the same bulk Cr fraction) according to the Wynblatt-Ku model (Fig. 5C). More interestingly, Γ_{Cr} in $Cr_{0.35}Mn_{0.2}Fe_{0.2}Co_{0.2}Ni_{0.05}$ can reach ~3.5 ML (Fig. 5D) *vs.* only <0.3 ML in $Cr_{0.35}Ni_{0.65}$ according to the binary Wynblatt-Ku model[7] (Fig. 5C). In summary, it is clear that the binary regular solution model cannot capture all trends of the complex adsorption behaviors in HEAs.

We further note that Wynblatt-Ku model[7] is further generalized to a multilayer adsorption model by Wynblatt and Chatain (noted as the Wynblatt-Chatain model).[5]

A further generalization of the Fowler-Guggenheim model for multicomponent alloys is the Guttmann model,[11] which use the segregation $\Delta H_{ads(i\to 1),0} - 2\alpha_{ii}X_i^{GB} + \sum_{j=2\ldots N;\, j\neq i} \alpha'_{ij} X_j^{GB}$ (to replace

the term " $\Delta H_0^{\mathrm{Seg}} + \omega z X^{\mathrm{GB}}$ " in Eq. (S9)), where $\Delta H_{ads(i\to 1),0} \approx \Delta G_{ads(i\to 1),0}$ is the intrinsic segregation enthalpy of the *i*-th component (with respect to Component 1), α_{ii} denotes the interaction between the 1-st and *i*-th complements, and α'_{ij} ($\alpha'_{ij} \equiv \alpha_{ij} - \alpha_{i1} - \alpha_{j1}$; $i \neq j$, $j \neq 1$) denotes the relative interaction between *i*-th and *j*-th components. However, the Guttmann model does not give a simple way to estimate parameters α_{ii} and α'_{ij}. Thus, we instead use either the binary approximation or Eq. (S15) in Supplementary Discussion 9 to compare with our MC/MD-simulated data.

It is important to note that these models do not consider entropic effects, multilayer adsorption, and different segregation free energies at different sites (including the effects of GB disorder), which are important and can affect GB segregation substantially.

Thus, none of these simplified models is sufficient, which justifies the usefulness of the new PIDDM developed based on the large-scale MC/MD simulations.

Specifically, the entropic effects of GB segregation have been considered in prior studies of binary and ternary alloys.[12, 13] In Supplementary Discussion 12, we will show an entropic effect of the segregation in this five-component system. Here, we have discovered a critical (compensation) temperature T_{C} due to an (incomplete) enthalpy-entropy compensation effect in the new PIDDM developed based on a careful analysis of the large dataset from the MC/MD simulations.

Table S3. Summary for all binary enthalpies of mixing ($\Delta H_{i,j}^{\mathrm{Mix}}$) and segregation ($\Delta H_{i,j}^{\mathrm{Seg}}$) for each of the binary alloys in CrMnFeCoNi based on the Miedema model, where we adopt *i* as solute and *j* as solvent. The data were extracted from Murdoch *et al.*.[10] Note that $\Delta H_{i,j}^{\mathrm{Mix}} \approx \Delta H_{j,i}^{\mathrm{Mix}}$ (the slight difference is due to the different formulae based on in the dilute solution limit in the Miedema model) but $\Delta H_{i,j}^{\mathrm{Seg}} \neq \Delta H_{j,i}^{\mathrm{Seg}}$. In our calculations for Cr segregation, Cr is the solute/segregating element. In our sign convention, a negative $\Delta H_{i,j}^{\mathrm{Seg}}$ indicates a preference for segregation, which is the opposite of the sign convention used by Schuh and co-workers.[10] Thus, we list the values of $\left(-\Delta H_{i,j}^{\mathrm{Seg}}\right)$ in this table; here, positive $\left(-\Delta H_{i,j}^{\mathrm{Seg}}\right)$ indicates segregation.

Binary Alloy (i, j)	$\Delta H_{i,j}^{\mathrm{Mix}}$ (J/mol)[a]	$\left(-\Delta H_{i,j}^{\mathrm{Seg}}\right)$(J/mol)[b]
Co, Fe	-1302	243
Cr, Fe	-5919	3737
Mn, Fe	1057	16605
Ni, Fe	-4922	2124
Fe, Co	-1231	-527
Mn, Co	-20046	13781
Ni, Co	-951	2237
Cr, Co	-16450	2720
Co, Ni	-950	-2473
Cr, Ni	-24788	-728
Fe, Ni	-4765	-3357
Mn, Ni	-31712	10005
Co, Mn	-18827	-18154
Fe, Mn	1510	-16222
Ni, Mn	-30160	-17223
Cr, Mn	8600	-11652
Co, Cr	-16469	-1485
Fe, Cr	-5874	-1676
Mn, Cr	8525	15095
Ni, Cr	-24868	-233

a. $\Delta H_{i,j}^{\mathrm{Mix}} = 0.71 \cdot \frac{1}{3}[-\Delta H_{i \text{ in } j}^{\mathrm{int}} - c_o \gamma_j^S V_j^{\frac{2}{3}} + c_o \gamma_i^S V_i^{\frac{2}{3}}]$, where $\Delta H_{i \text{ in } j}^{\mathrm{int}}$ is chemical interaction term, c_o is constant, $\gamma_{i(j)}^S$ is surface energy of *i*(*j*), and $V_{i(j)}$ is atomic volume of *i*(*j*). Here, the $c_o \gamma_{i(j)}^S V_{i,(j)}^{\frac{2}{3}}$ term represents the surface enthalpy of pure metal as defined in the Miedema model.

b. $\left(-\Delta H_{i,j}^{\mathrm{Seg}}\right) = -\Delta H_{i,j}^{\mathrm{Mix}} + \Delta E_{el}$, where ΔE_{el} is the elastic interaction. Here, positive $\left(-\Delta H_{i,j}^{\mathrm{Seg}}\right)$ indicates segregation (noting that our sign convention differs from that used by Murdoch *et al.*[10]).

Supplementary Discussion 8: Discussion of a density-based thermodynamic model

Recently, Li *et al.* proposed a density-based thermodynamic model for GB segregation in HEAs.[14] This phenomenological model assumed that GB energy (E_{GB}) can be expressed as:

$$E_{GB} = a_0 \cdot (1-\rho_{GB})^2, \quad \text{(S12)}$$

where a_0 is a materials constant and ρ_{GB} is the GB density. Here, the ρ_{GB} is a characteristic property of the GB and it should be closely related to GB free volume $V_{Free} \propto (1- \rho_{GB})$. In other words, V_{Free} is considered as a key factor to affect GB segregation in this density-based thermodynamic model.

However, the correlation analysis based on the 1032 MC/MD simulations indicates that GB excess of disorder (Γ_{Dis}) can strongly affect GB segregation in HEAs, but the GB free volume (V_{Free}) always has weak correlations with any GB adsorption properties; see more discussion in Supplementary Discussion 2. Thus, this suggests that the GB disorder parameter, instead of the GB density or free volume, is the dominant parameter influencing GB segregation.

Supplementary Discussion 9: A generalized lattice-type model for GB segregation in HEAs

A lattice-type model has been developed for GB segregation in ternary alloys.[9] In this model, the segregation enthalpy of C atoms in a ternary ABC alloy can be expressed as a function of binary enthalpies of segregation and mixing, extending from a binary AC alloy, as:

$$\left(-\Delta H_{AB-C}^{Seg-eff}\right) = \left(-\Delta H_{AC}^{Seg(bin)}\right) + a\Delta H_{AB}^{Mix} - b\Delta H_{AC}^{Mix} - c\Delta H_{BC}^{Mix}, \quad \text{(S13)}$$

where $\Delta H_{AC}^{Seg(bin)}$ is the segregation enthalpy of C in a binary AC alloy, ΔH_{AB}^{Mix}, ΔH_{AC}^{Mix}, and ΔH_{BC}^{Mix} are mixing enthalpies of A-B, A-C, and B-C, respectively, and constants a, b, and c ($0 < a, b, c < 1$) depend on the coordination numbers.[9] Here, we again note that a negative $\Delta H_{i,j}^{\mathrm{Seg}}$ indicates a preference for segregation In our sign convention, which is the opposite of the sign convention used by Schuh's group (Murdoch *et al.*[10] and Xing *et al.*[9]). Thus, we use $\left(-\Delta H_{i,j}^{\mathrm{Seg}}\right)$ in some equations and Fig. S12, where positive $\left(-\Delta H_{i,j}^{\mathrm{Seg}}\right)$ indicates segregation. In the above equation, the enthalpies of mixing can intuitively affect the segregation enthalpy. For example, positive ΔH_{AB}^{Mix} implies that GB segregation of C atoms may be favorable because it reduces the density of unfavorable A-B bonds at the GB. Moreover, negative ΔH_{AC}^{Mix} or ΔH_{BC}^{Mix} may promote the GB segregation of C atoms to increase the density of favorable A-C or B-C bonds at the GB.

We may extend the above equation to a quinary HEA, where the segregation enthalpy of E in quaternary ABCDE alloy can be expressed as:

$$\left(-\Delta H_{ABCD-E}^{Seg-eff}\right) = \frac{\left(-\Delta H_{AE}^{Seg(bin)}\right)+\left(-\Delta H_{BE}^{Seg(bin)}\right)+\left(-\Delta H_{CE}^{Seg(bin)}\right)+\left(-\Delta H_{DE}^{Seg(bin)}\right)}{4}$$

$$+\frac{a\left(\Delta H_{AB}^{Mix}+\Delta H_{AC}^{Mix}+\Delta H_{AD}^{Mix}+\Delta H_{BC}^{Mix}+\Delta H_{BD}^{Mix}+\Delta H_{CD}^{Mix}\right)}{6} - \frac{b\left(\Delta H_{AE}^{Mix}+\Delta H_{BE}^{Mix}+\Delta H_{CE}^{Mix}+\Delta H_{DE}^{Mix}\right)}{4}, \quad \text{(S14)}$$

where the first term is the averaged binary segregation enthalpy of E in A, B, C, and D (assuming an equimolar solid solution for simplicity), the second term is the averaged binary enthalpy of mixing of any two elements in A, B, C, and D, the thrid term is the averaged binary enthalpy of mixing of E with A, B, C, and D, and constants α and b are coefficients ranged between 0 and 1.

Using this equation, we can estimate the segregation enthalpies of each element in the CrMnFeCoNi cantor alloy. The binary segregation enthalpies and mixing enthalpies can be found

in Ref. [10], and we have tabulated all data in Table S1 for convenience. Since a and b are unknown, we first test constant a and b based on prior experiments [9]. Here, three sets of a and b are chosen: a = 1/3 and b = 1/3, a = 1/6 and b = ½, and a = 0 and b = 1. The calculated segregation enthalpies for each set are shown in Fig. S12 for comparison. By comparing with two experimentally characterized GBs from prior studies [2, 3] in Fig. S12(d), we found that the calculated segregation enthalpies (ΔH_{Seg}) using a = 1/6 and b = ½ (Fig. S12(b)) have the best agreement with experiments, where Cr, Mn, and Ni have positive ΔH_{Seg} (segregation), while Fe and Co have negative ΔH_{Seg} (depletion at GB).

To further validate this generalized lattice model, we compute segregation enthalpies for selected non-equimolar HEAs. In this case, since each element may have different contribution to segregation, we take weigtht coeffient w into account to refine Eq. (S14):

$$\left(-\Delta H_{ABCD-E}^{Seg-eff}\right) = \frac{w_{AE}\left(-\Delta H_{AE}^{Seg(bin)}\right)+w_{BE}\left(-\Delta H_{BE}^{Seg(bin)}\right)+w_{CE}\left(-\Delta H_{CE}^{Seg(bin)}\right)+w_{DE}\left(-\Delta H_{DE}^{Seg(bin)}\right)}{w_{AE}+w_{BE}+w_{CE}+w_{DE}}$$
$$+\frac{a\left(w_{AB}\Delta H_{AB}^{Mix}+w_{AC}\Delta H_{AC}^{Mix}+w_{AD}\Delta H_{AD}^{Mix}+w_{BC}\Delta H_{BC}^{Mix}+w_{BD}\Delta H_{BD}^{Mix}+w_{CD}\Delta H_{CD}^{Mix}\right)}{w_{AB}+w_{AC}+w_{AD}+w_{BC}+w_{BD}+w_{CD}}$$
$$-\frac{b\left(w_{AE}\Delta H_{AE}^{Mix}+w_{BE}\Delta H_{BE}^{Mix}+w_{CE}\Delta H_{CE}^{Mix}+w_{DE}\Delta H_{DE}^{Mix}\right)}{w_{AE}+w_{BE}+w_{CE}+w_{DE}}, \quad \text{(S15)}$$

where we assume $w_{AB(C,D)} = \frac{X_A+X_{B(C,D)}}{2}$ and X's are bulk compositions[9]. Take the CrMnFeCoNi HEA as one example, the weight coefficient of Cr and Mn (w_{CrMn}) can be determined by $w_{CrMn} = \frac{X_{Cr}+X_{Mn}}{2}$, where X_{Cr} and X_{Mn} are the bulk composition of Cr and Mn.

In addition, we can compare the model-estimated $\left(-\Delta H_{Seg}^{Cr}\right)$ and MC/MD-simulated Γ_{Cr} in $Co_{0.2}Mn_xNi_xFe_{0.4-x}Co_{0.4-x}$ as a function of both Mn and Ni bulk compositions ($x = X_{\mathrm{Mn}} = X_{\mathrm{Ni}}$). Figs. S13(c) and S13(d) show that both model-calculated $\left(-\Delta H_{Seg}^{Cr}\right)$ and MC/MD-simulated Γ_{Cr} increase with decreasing x (= X_{Mn} = X_{Ni}). Specifically, with increasing Ni content in the alloy, $\left(-\Delta H_{Seg}^{Cr}\right)$ decreases from -2.99 kJ/mol in $Cr_{0.2}Mn_{0.35}Fe_{0.05}Co_{0.2}Ni_{0.2}$ to -3.01 kJ/mol in $Cr_{0.2}Mn_{0.35}Fe_{0.05}Co_{0.05}Ni_{0.35}$ (Fig. S8a and 8c); meanwhile, Γ_{Cr} decreases from 6 nm^{-2} to 4 nm^{-2} (Fig. S13(b) and 13(d)). Moreover, with decreasing the Ni content, the $\left(-\Delta H_{Seg}^{Cr}\right)$ increases from 6.45 kJ/mol in $Cr_{0.2}Mn_{0.05}Fe_{0.35}Co_{0.2}Ni_{0.2}$ to 6.48 kJ/mol in $Cr_{0.2}Mn_{0.05}Fe_{0.35}Co_{0.35}Ni_{0.05}$ (Fig. S13(a) and S13(c)), while Γ_{Cr} increases from 31 nm^{-2} to 43 nm^{-2} (Fig. S13(b) and S13(d)). These

agreements again suggest that the lattice model predictions are consistent with our simulations. Lastly, prior results [2] also indicate that Mn and Ni may compete the segregation sites with Cr, but Fe and Co promote Cr segregation, which is also consistent with our simulations and analysis discussed in Supplementary Discussion 4.

Although the lattice model can predict segregation trends, the predictions are not quantitatively accurate (given the simplifications adopted by the model). As an example, we list the calculated $\left(-\Delta H_{Seg}^{Cr}\right)$ of non-equimolar HEA1-4 in Table 1 (where HEA1-3 has strong Cr segregation but HEA4 has weak Cr segregation) and plot the $\left(-\Delta H_{Seg}^{Cr}\right)$ as a function of a and b for Σ13, Σ15, Σ41, and Σ81 GBs in Fig. S14. However, we cannot identify a region where $\left(-\Delta H_{Seg}^{Cr}\right)$ of HEA1-3 > HEA4 (Fig. S14). This suggests that the lattice model cannot quantitatively represent this case. This is no surprise since the lattice model is simplified and it cannot capture the complex interactions of segregation of multiple elements, GB disorder, and their coupling effects.

Again, the entropic effects of GB segregation, which are important,[12, 13] have not been considered in this simplified model. In Supplementary Discussion 12, we will show an (incomplete) enthalpy-entropy compensation effect in the new PIDDM developed based on the large dataset from the MC/MD simulations, which was not captured in this simplified model that only considers segregation enthalpies (that already becomes complicated for a five-component system).

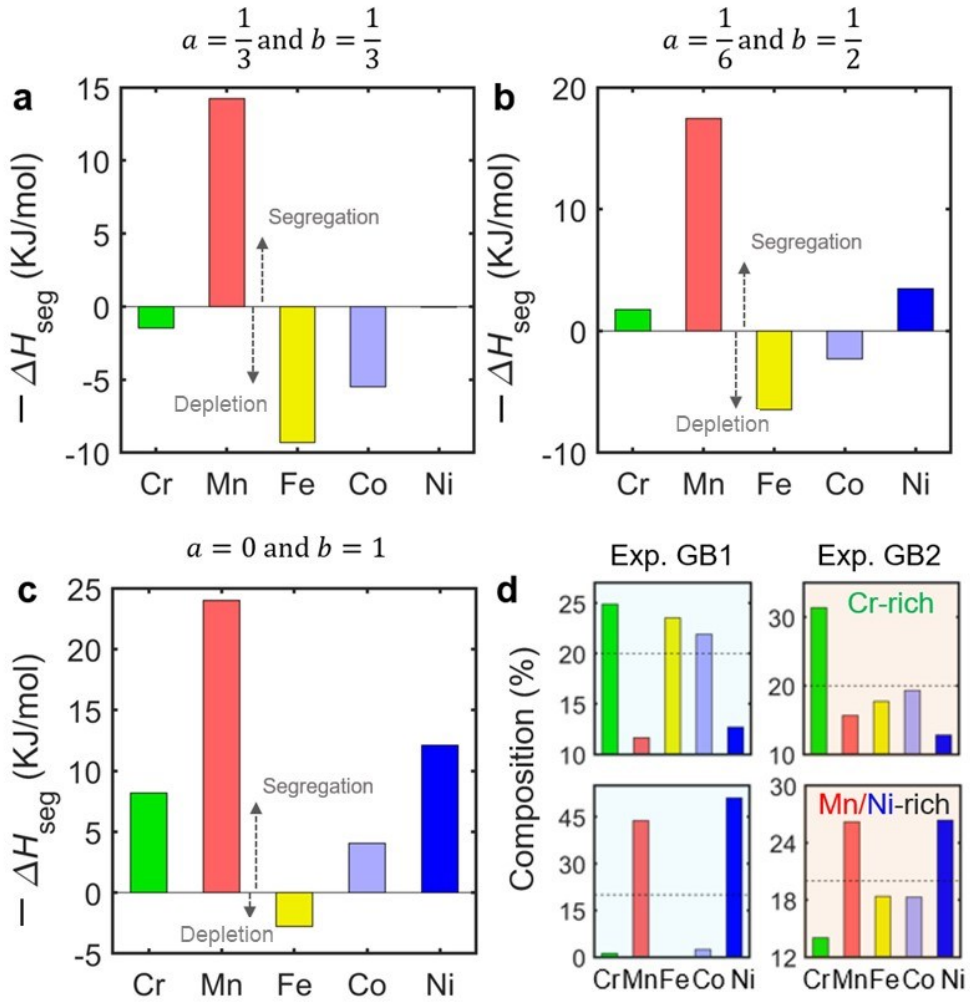

Fig. S12. Calculated segregation enthalpies (ΔH_{Seg}) of each element based on the generalized lattice-type model with different coefficients a and b. (**a**) a = 1/3 and b = 1/3, (**b**) a = 1/6 and b = ½, and (**c**) a = 0 and b = 1. Here, a positive $\left(-\Delta H_{\mathrm{Seg}}\right)$ or negative ΔH_{Seg}^{Cr} suggests GB segregation, while a negative $\left(-\Delta H_{\mathrm{Seg}}\right)$ suggests GB depletion. (**d**) Selected measured compositions at (randomly selected) general GBs from APT. The upper panel shows the measured GB composition at a Cr-rich GB region (from Ref. 2, for a GB annealed at 450 °C) and bottom panel shows that at a Mn and Cr-rich GB (from Ref. 3, for a randomly selected GB annealed at 700 °C). Note that the calculated $\left(-\Delta H_{\mathrm{Seg}}\right)$ by using a = 1/6 and b = ½ has the best agreement with experiments, where Co, Mn, and Ni segregate at GBs, with GB depletion of Fe and Co. Again, we note that a negative ΔH_{Seg} indicates a preference for segregation in our sign convention. Here, we use $\left(-\Delta H_{\mathrm{Seg}}\right)$ in this figure, where positive $\left(-\Delta H_{\mathrm{Seg}}\right)$ indicates segregation.

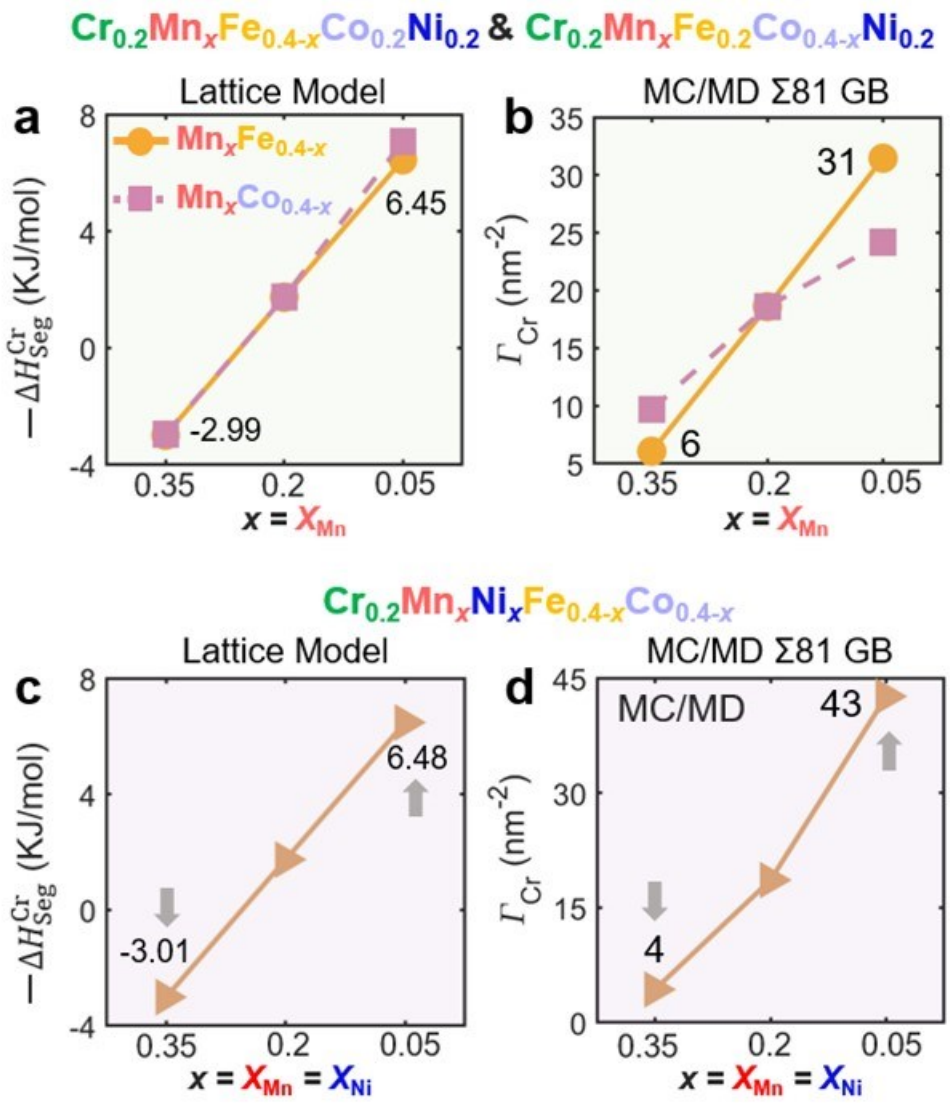

Fig. S13. Prediction of the GB segregation in non-equimolar HEAs using the lattice-type model. (**a**) Calculated segregation enthalpies of Cr ($-\Delta H_{\mathrm{Seg}}^{\mathrm{Cr}}$) *vs.* **b**, MC/MD-simulated Γ_{Cr} as functions of bulk Mn fraction for $Cr_{0.2}Mn_xFe_{0.4-x}Co_{0.2}Ni_{0.2}$ and $Cr_{0.2}Mn_xFe_{0.2}Co_{0.4-x}Ni_{0.2}$. (**c**) Calculated $\left(-\Delta H_{\mathrm{seg}}\right)$ for Cr *vs.* (**d**) MC/MD-simulated Γ_{Cr} as functions of the bulk Mn/Ni fraction ($x = X_{\mathrm{Mn}} = X_{\mathrm{Ni}}$) for $Cr_{0.2}Mn_xNi_xFe_{0.4-x}Co_{0.4-x}Ni_{0.2}$. The grey arrows indicate variations compared to the Ni-fixed case in shown in Panel (a) and (b). Again, we note that a negative ΔH_{Seg} indicates a preference for segregation in our sign convention. Here, we use $\left(-\Delta H_{\mathrm{Seg}}\right)$ in this figure, where positive $\left(-\Delta H_{\mathrm{Seg}}\right)$ indicates segregation.

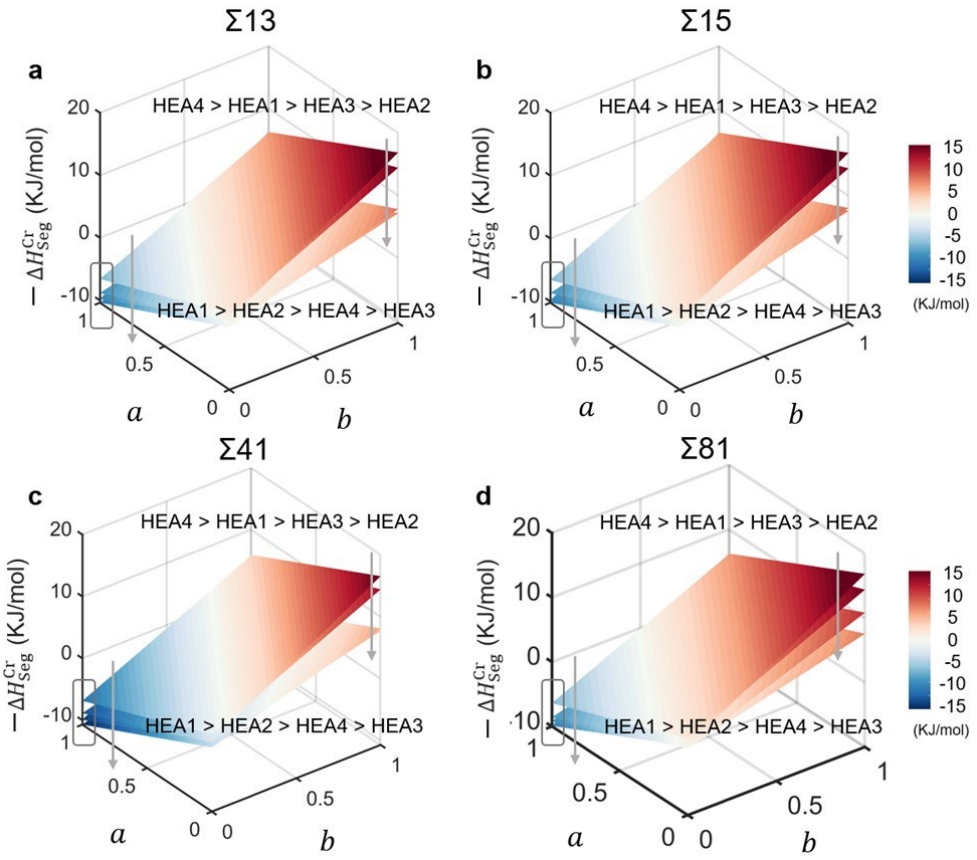

Fig. S14. Further testing of the lattice-type model for the Cr segregation in non-equimolar HEAs. Calculated segregation enthalpies of Cr ($\Delta H_{\mathrm{Seg}}^{\mathrm{Cr}}$) for (**a**) Σ13, (**b**) Σ15, (**c**) Σ41, and (**d**) Σ81 GBs as functions of coefficients a and b. The HEA1-3 are non-equimolar HEAs with strong Cr segregation, and HEA4 is weak Cr-segregation alloy (see Table S4 for detail). The bulk compositions for each GB based on MC/MD simulations are used to calculate $\Delta H_{\mathrm{Seg}}^{\mathrm{Cr}}$. For all four GBs, we cannot identify a region where $\left(-\Delta H_{\mathrm{Seg}}^{\mathrm{Cr}}\right)$ of HEA1-3 > HEA4. Even under two extreme conditions: (1) $a = 0$ and $b = 1$, calculated $\Delta H_{\mathrm{Seg}}^{\mathrm{Cr}}$ has the order of HEA4 > HEA1 > HEA3 > HEA2 relations, (2) $a = 1$ and $b = 0$, $\left(-\Delta H_{\mathrm{Seg}}^{\mathrm{Cr}}\right)$ has the order HEA1 > HEA2 > HEA4 > HEA3 relations. Therefore, the lattice model cannot quantitatively represent the segregation in these non-equimolar HEAs. Again, we note that a negative ΔH_{Seg} indicates a preference for segregation in our sign convention. Here, we use $\left(-\Delta H_{\mathrm{Seg}}^{\mathrm{Cr}}\right)$ in this figure, where positive $\left(-\Delta H_{\mathrm{Seg}}^{\mathrm{Cr}}\right)$ indicates segregation.

Supplementary Discussion 10: The generality of predicted Cr segregations at different GBs by MC/MD simulations and DFT validations

To verify the generality of GB segregation in the Σ81 mixed GB HEA, we further performed MC/MD simulations for three other GBs, including a Σ15 asymmetric GB, a Σ41 tilt GB, and a Σ13 twist GB, in four selected non-equimolar HEAs (HEA1-4, as listed in Table S4).

The MC/MD-calculated Γ_{Cr} of HEA1-4 for each GB at 1000 K are tabulated in Table S4, which shows that the Γ_{Cr} values of HEA1-3 are significantly larger than that of HEA4 for all GBs. By plotting the averaged Cr compositional profile along the direction perpendicular to GB, we can observe that Cr has strong accumulation at the GB region for HEA1-3, but weak enrichment in HEA4 at all four GBs. Therefore, the GB segregation behaviors observed in Σ81 GB, which are qualitatively reproduced in three other GBs, is representative for general GBs (but we recognize that the quantitative segregation amounts can vary and high-symmetry low-Σ GBs can behave differently).

Furthermore, we carried out DFT calculations to further verify the predicted Cr segregation in HEA GBs. Since the minimal cell of Σ81 GB is too large (>1000 atoms) to perform DFT calculations, we used a Σ15 GB with 288 atoms to calculate segregation energy of Cr: $E_{\mathrm{Seg}}^{\mathrm{Cr}} = (E_{\mathrm{Cr@GB}} - E_{\mathrm{Cr@bulk}})/N_{\mathrm{Cr}}$, where $E_{\mathrm{Cr@GB}}$ is the energy of Cr at GB, $E_{\mathrm{Cr@bulk}}$ is the energy of Cr at bulk, and N_{Cr} is total number of Cr atom. To minimize the errors, we randomly generated five different GB structures with (strong) Cr segregation and other five different GB structures without (or with little) Cr segregation for HEA1-4. The final $E_{\mathrm{Seg}}^{\mathrm{Cr}}$ was the average based on these structures. Finally, the calculated $E_{\mathrm{Seg}}^{\mathrm{Cr}}$ values range from -23.6 to -28.3 meV/atom for HEA1-3, which is significantly lower than the calculated $E_{\mathrm{Seg}}^{\mathrm{Cr}}$ of ~ 0.1 meV/atom for HEA4. Therefore, the DFT calculations support and validate the predictions of our MC/MD simulations.

Table S4. Comparison of the MC/MD-simulated asymmetric Σ81 GB with three other types of GBs. On the one hand, HEA1-3 are non-equimolar HEAs with strong Cr segregation (large Γ_{Cr}) and large disorder (Γ_{Dis}) based on the simulations of the Σ81 asymmetric GB and ANN-prediction. On the other hand, HEA4 has weak Cr segregation and small disorder. Similar segregation trends have been observed for the asymmetric Σ15 GB, tilt Σ41GB, and Σ13 twist GB, where HEA1-3 have larger Γ_{Cr} and Γ_{Dis} than HEA4. The Γ_{Cr} and Γ_{Dis} were calculated from MC/MD-simulated GB structures at 1000 K. A detailed comparison of GB structures was shown in Fig. S15.

	Composition	Σ81 Mixed. GB[a]		Σ15 Asym. GB		Σ41 Tilt GB		Σ13 Twist GB		DFT[b] E_{Seg}^{Cr} (meV/atom)
		Γ_{Cr} (nm^{-2})	Γ_{Dis} (nm^{-2})	Γ_{Cr} (nm^{-2})	Γ_{Dis} (nm^{-2})	Γ_{Cr} (nm^{-2})	Γ_{Dis} (nm^{-2})	Γ_{Cr} (nm^{-2})	Γ_{Dis} (nm^{-2})	
HEA1	$Cr_{0.2}Mn_{0.05}Fe_{0.35}Co_{0.2}Ni_{0.2}$	31	41	69	64	107	42	44	32	-28.3
HEA2	$Cr_{0.2}Mn_{0.2}Fe_{0.35}Co_{0.2}Ni_{0.05}$	44	49	60	68	108	58	23	30	-23.6
HEA3	$Cr_{0.25}Mn_{0.2}Fe_{0.25}Co_{0.2}Ni_{0.10}$	45	47	42	61	101	37	26	32	-24.7
HEA4	$Cr_{0.20}Mn_{0.05}Fe_{0.2}Co_{0.2}Ni_{0.35}$	4	37	15	58	14	31	12	31	0.1

a. ANN models were developed from Σ81 mixed GB.

b. DFT calculations were based on ten random configurations with and without Cr segregation using a small Σ15 asymmetric GB with 288 atoms.

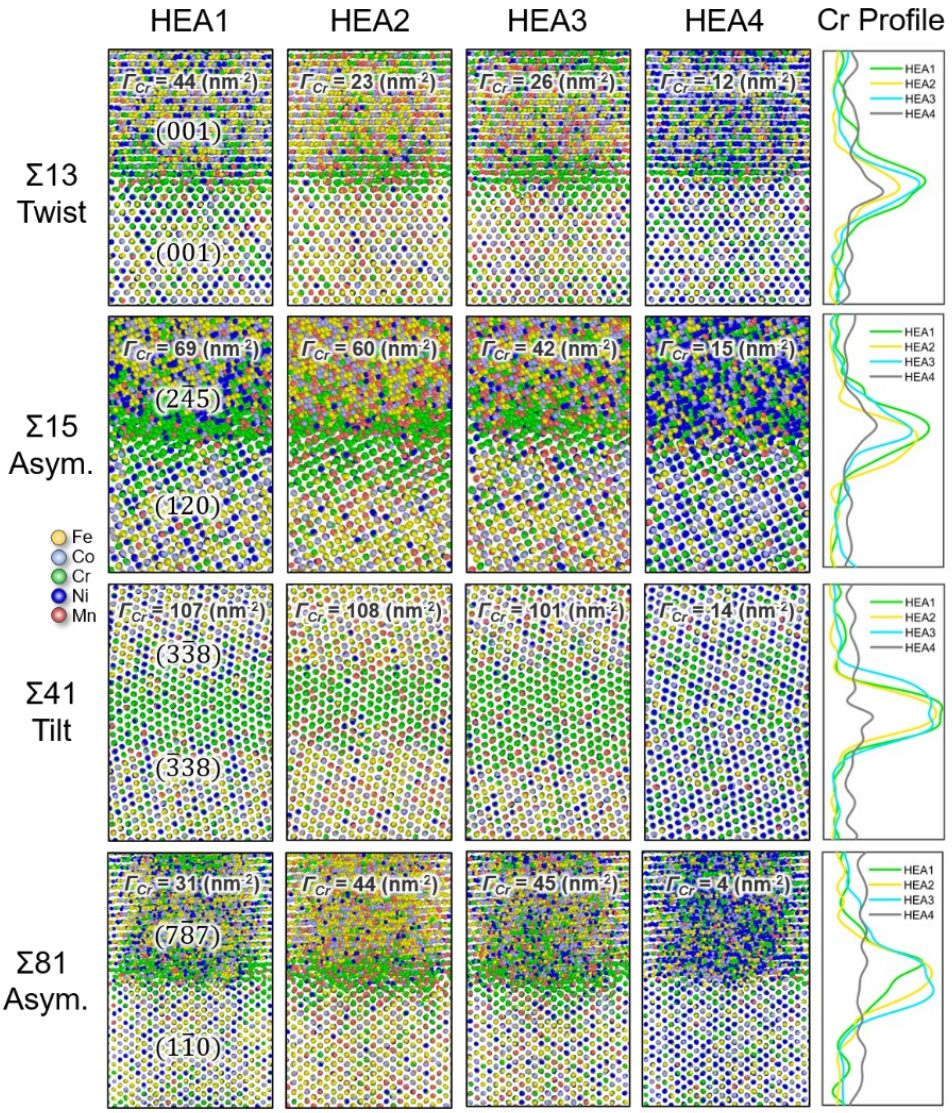

Fig. S15. Screenshots of MC/MD-simulated GB structures at 1000 K for four different GBs in four selected non-equimolar HEAs. The right panels are Cr distribution profiles perpendicular to the GB direction. For all four types of GB, HEA1-HEA3 have larger GB excess of Cr adsorption (Γ_{Cr}) than HEA4 (see Table 1 in the main text for detail), and corresponding Cr profiles confirming the stronger Cr segregation at HEA1-3 GBs than HEA4 in all cases.

Supplementary Discussion 11: First-principles calculations of the sum of bond ordering (SBO)

The sum of bond ordering (SBO) has been calculated for each random GB structures of HEA1-4 following the all-electron static calculations using the DDEC06 method [15]. For structures with both strong and weak Cr segregation in HEA1-4, the averaged SBO for each atom almost remains the same. Therefore, the final SBO value is averaged based on 10 different GB structures. Fig. S23 shows the averaged SBO of each element in CrMnFeCoNi with error bars. The calculated averaged SBOs for Fe (~4.04), Cr (~3.95), and Co (~3.78) are similar. However, Mn and Ni exhibit two different averaged SBOs, which are ~4.2 and ~3.5, respectively. Since SBO represents the total number of electrons that form bonds, the similar SBO values indicate similar chemical bonding environment. Thus, the strong segregation of Cr at Fe and Co-rich GBs can be further ascribed to the similar bonding environments, while the weak segregation of Cr and Mn and Ni-rich GBs can be attributed to the different bonding environments.

Notably, a recent study showed that a large chemical affinity disparity will induce strong atomic segregation and short-range ordering in HEAs.[16] This chemical-affinity analysis is consistent with our SBO calculations.

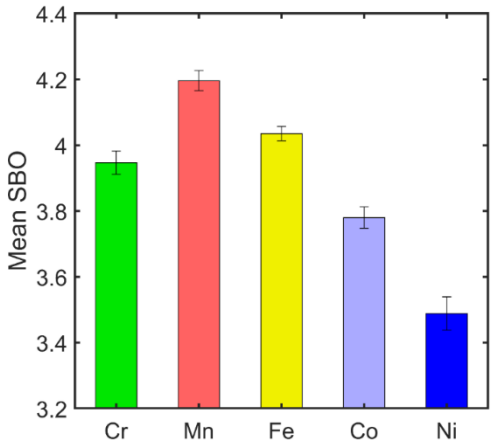

Fig. 16. Means of sum of bond ordering (SBO) for each element in the HEAs. The SBO has been calculated based on 10 different GB structures (five different GB structures with strong Cr segregation and other five GB structures without Cr segregation), and final SBO values are averaged based on 40 GB structures (10 different GB structures × four non-equimolar HEA1-4). The similar SBOs indicate similar bonding environments. The concept of SBOs may also provide new insights on tailoring GB segregation for HEA. For example, if we want to promote segregation of certain element (*e.g.*, Cr), we may increase the number of elements with similar SBOs (*e.g.*, Fe and Co) and reduce the elements with different SBOs (*e.g.*, Mn and Ni).

Supplementary Discussion 12: Discussion of the physical meaning and origin of the critical (isoequilibrium) temperature T_C

On the one hand, Eq. (S3) of the PIDDM in Supplementary Discussion 6 can be rewritten as:

$$\Gamma_i(T,X) = \Delta\Gamma_{Dis} \cdot \beta_i \cdot (T - T_C) + \Gamma_i^0(X)\,, \tag{S16}$$

where $\Delta\Gamma_{Dis} \equiv [\Gamma_{Dis}(T,X) - \Gamma_{\mathrm{Dis}}^0] \approx \left[\Gamma_{Dis}(T,X) - \Gamma_{\mathrm{Dis}}^{\min}\right]$ is the net increased GB disorder induced by segregation and/or temperature from the minimum level. If $\Gamma_i^0(X)$ can be neglected (because $\Gamma_i^0 = \langle\Gamma_i^0(X)\rangle$ is small as shown in Fig. 10(a-d)), we have the following approximation at $T = T_C$:

$$\Gamma_i(T_C,X) = \Gamma_i^0(X) \sim 0. \tag{S17}$$

Thus, this T_C is the "isoequilibrium" temperature of GB segregation due an enthalpy-entropy compensation.[5, 17, 18] Interestingly, the fitted T_C values are almost the same for all elements ($T_C \approx 1388 \pm 51$ K with a moderate difference for Mn with a small slope; it is difficult to determine T_C accurately for Ni with an almost zero slope), as shown in Fig. S10(f) (or the Fig 4*D* in the main article).

On the other hand, we may understand the physical meaning of this critical temperature T_C based on a multicomponent segregation model that consider both segregation enthalpy and entropy (yet a simplified lattice-occupying model, assuming all GB sites are identical for simplicity, to reveal the physical origin of T_C):

$$\frac{X_i^{\mathrm{GB}}}{X_1^{\mathrm{GB}}} = \frac{X_i^{\mathrm{Bulk}}}{X_1^{\mathrm{Bulk}}} exp\left(-\frac{\Delta G_{i\to 1}^{\mathrm{Seg}}}{k_B T}\right), \tag{S18}$$

where X_i^{GB} and X_i^{Bulk} are the fractions of solute element *i* at the GB and bulk, respectively, *i* = 1 is a "reference" element (*e.g.*, we may Ni with little segregation in this case for convenience, though it can be any element), and $\Delta G_{i\to 1}^{\mathrm{Seg}}$ is the free energy of segregation by swapping of a solute element *i* inside the bulk (grain) with an element 1 at the GB. This simplified model suggests that the segregation of all elements can simultaneously vanish at T_C if:

$$\Delta G_{i\to 1}^{\mathrm{Seg}} = \Delta H_{i\to 1}^{\mathrm{Seg}} - T_C \cdot \Delta S_{i\to 1}^{\mathrm{Seg}} = 0, \tag{S19}$$

which will lead to $X_i^{\mathrm{GB}} = X_i^{\mathrm{Bulk}}$ for all elements, or $\Gamma_i(T_C,X) = 0$.

For realistic modelling of HEAs (via MC/MD simulations or the PIDDM), we cannot identify single values of segregation enthalpies and entropies. Nonetheless, the observation of almost identical $T_{\mathrm{C}} \approx 1388 \pm 51$ K for all elements, as shown in Fig. S10(f) and Table S2, suggests that the effective GB segregation entropy ($\Delta S_{i\to 1}^{\mathrm{Seg\,(eff)}}$) should be proportional to the effective GB segregation enthalpy ($\Delta H_{i\to 1}^{\mathrm{Seg(eff)}}$) to achieve an isoequilibrium effect[5, 17, 18] if:

$$\Delta H_{i\to 1}^{\mathrm{Seg(eff)}} = \Delta S_{i\to 1}^{\mathrm{Seg\,(eff)}} \cdot T_C + C, \tag{S20}$$

so that $\Delta G_{i\to 1}^{\mathrm{Seg(eff)}} = C$. In the current case, the constant C must vanish for a perfect isoequilibrium effect due to the network constrain ($\sum_i X_i^{\mathrm{Bulk}} = \sum_i X_i^{\mathrm{GB}} = 1$), albeit the enthalpy-entropy compensation may not be perfect (leading to small C_i that produces non-zero residual $\Gamma_i^0(X) = \sum_i\left(\kappa_i^{\mathrm{Dis}} \cdot X_i\right)$ term).

Note that "isoequilibrium" is the preferred term adopted here (*vs.* "compensation"[5]) to emphasize the existence of a common intersection point for all five elements in the adsorption equation based on the terminology discussion by Liu and Guo.[18]

Comparing with Eq. (S16) (or $\Gamma_i(T, X) = \Delta\Gamma_{Dis} \cdot \beta_i \cdot (T - T_{\mathrm{C}})$, assuming $\Gamma_i^0(X) \sim 0$), we conclude that this entropic effect must be related to the increased GB disorder $\Delta\Gamma_{Dis}$.

Although it is difficult to derive an analytical model for this critical (isoequilibrium) temperature T_{C}, we can now envision the following picture for its physical meaning and origin:

- The increased GB disorder $\Delta\Gamma_{Dis}$ can reduce the effective GB free energy of segregation ($\Delta G_{i\to 1}^{\mathrm{Seg(eff)}}$) through the entropy of GB segregation.
- This reduction in the effective $\Delta G_{i\to 1}^{\mathrm{Seg(eff)}}$ is (approximately) proportional to $\Delta H_{i\to 1}^{\mathrm{Seg(eff)}}$. In other words, this reduction is more significant for strong segregating/depleting elements.
- Thus, with increasing GB disorder $\Delta\Gamma_{Dis}$, the effective $\Delta G_{i\to 1}^{\mathrm{Seg(eff)}}$ values for different elements are reduced and equalized due to this entropic effect. The effective $\Delta G_{i\to 1}^{\mathrm{Seg(eff)}}$ almost vanishes (or is minimized) at T_{C}.

Finally, we again emphasize that it is unlikely that this compensation effect is rigorously held to produce an exactly identical T_{C} for all elements because (***i***) $\Gamma_i(X)$ is small, but it is not exactly

zero and (***ii***) Eq. (S19) is likely an approximation (*i.e.*, $\Delta S_{i\to 1}^{\mathrm{Seg\,(eff)}}$ likely scales with, but not is exactly proportional to $\Delta H_{i\to 1}^{\mathrm{Seg(eff)}}$). Instead, an approximated relation based on the above proposed physical mechanism can exist. Our data (Table S2 and Fig. S10(f)) also show variations in the specific T_{C} values for different elements, particularly for weak segregation systems:

- T_{C} = 1347 K for the strong segregating Cr.
- T_{C} = 1370 K for Fe, and T_{C} = 1371K for Co, both of which exhibit strong GB depletion.
- T_{C} = 1464 K for the weak segregating Mn (albeit a possible large error with a small slope).
- The mean is 1388 K, and the standard deviation is 51K.
- T_{C} cannot be determined for Ni because of a nearly zero slope.

Supplementary Discussion 13: Additional computed grain boundary (GB) diagrams

Additional computed grain boundary (GB) diagrams are documented:

- ✓ **Supplementary Figs. S17-S22** are ANN-predicted *vs*. hybrid MC/MD-simulated binary GB diagrams.
- ✓ **Supplementary Figs. S23-S29** are ANN-predicted ternary GB diagrams.

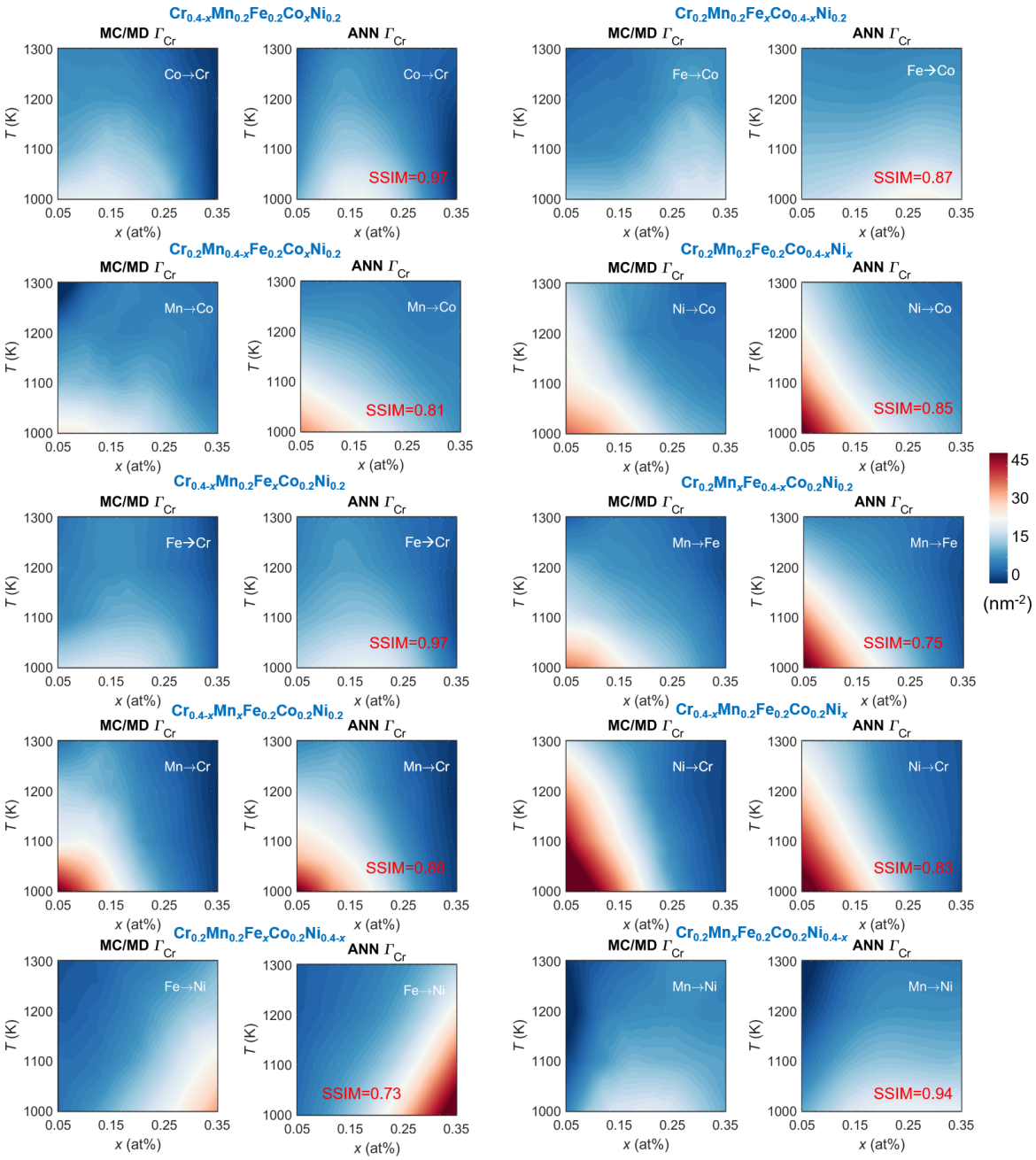

Fig. S17. 10 pairs of ANN-predicted *vs*. hybrid MC/MD-simulated diagrams of the GB excess of Cr (Γ_{Cr}).The label of "Co→Ni" indicates that the bulk Co fraction increases from x = 0.05 to 0.35 at%, while replacing Ni (the bulk Ni fraction = $0.4 - x$).

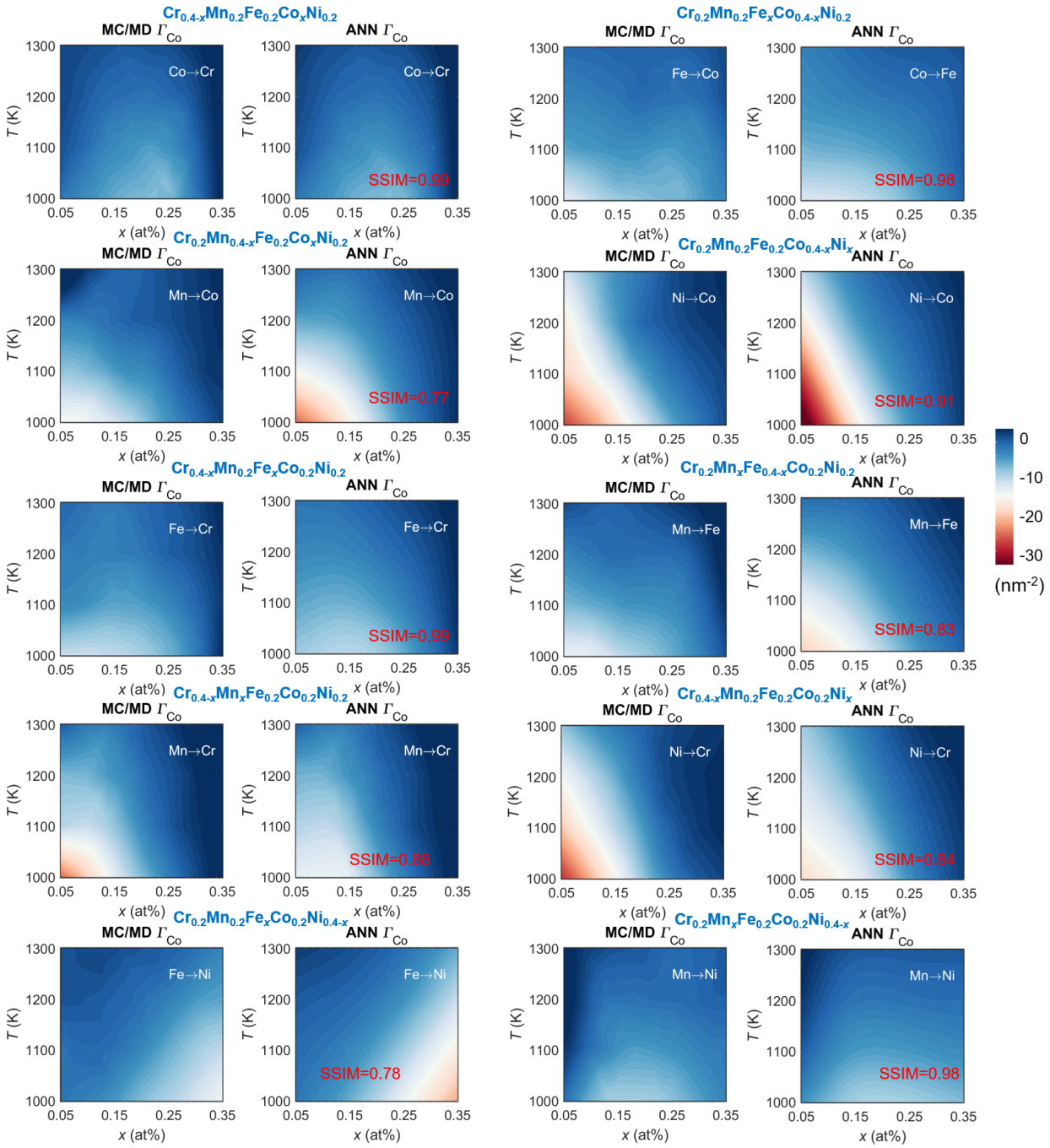

Fig. S18. 10 pairs of ANN-predicted *vs*. hybrid MC/MD-simulated diagrams of GB excess of Co (Γ_{Co}). The label of "Co→Ni" indicates that the bulk Co fraction increases from x = 0.05 to 0.35 at%, while replacing Ni (bulk Ni fraction = 0.4 $-$ x).

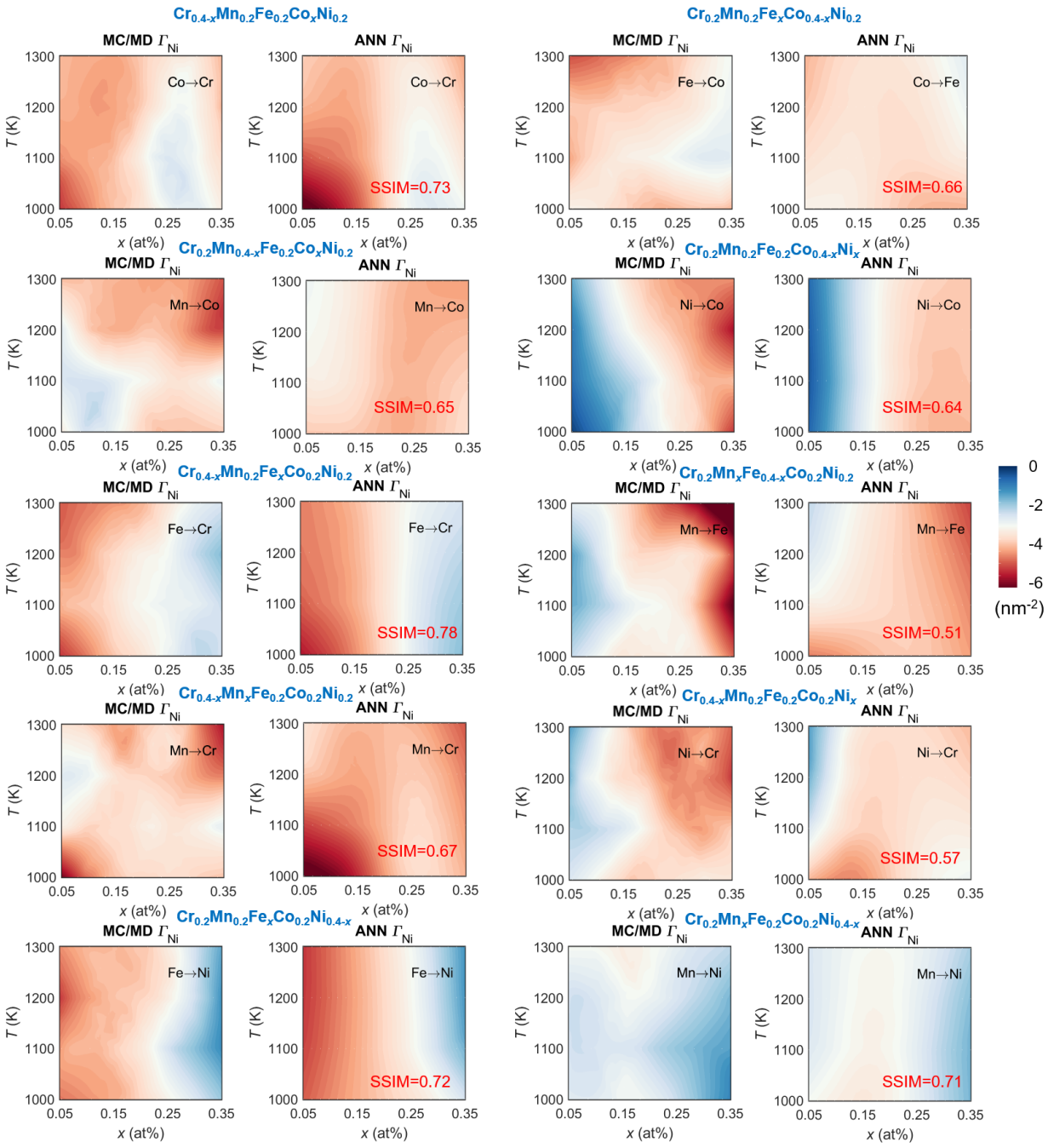

Fig. S19. 10 pairs of ANN-predicted *vs*. hybrid MC/MD-simulated diagrams of GB excess of Ni (Γ_{Ni}). The label of "Co→Ni" indicates that the bulk Co fraction increases from x = 0.05 to 0.35 at%, while replacing Ni (the bulk Ni fraction = $0.4 - x$).

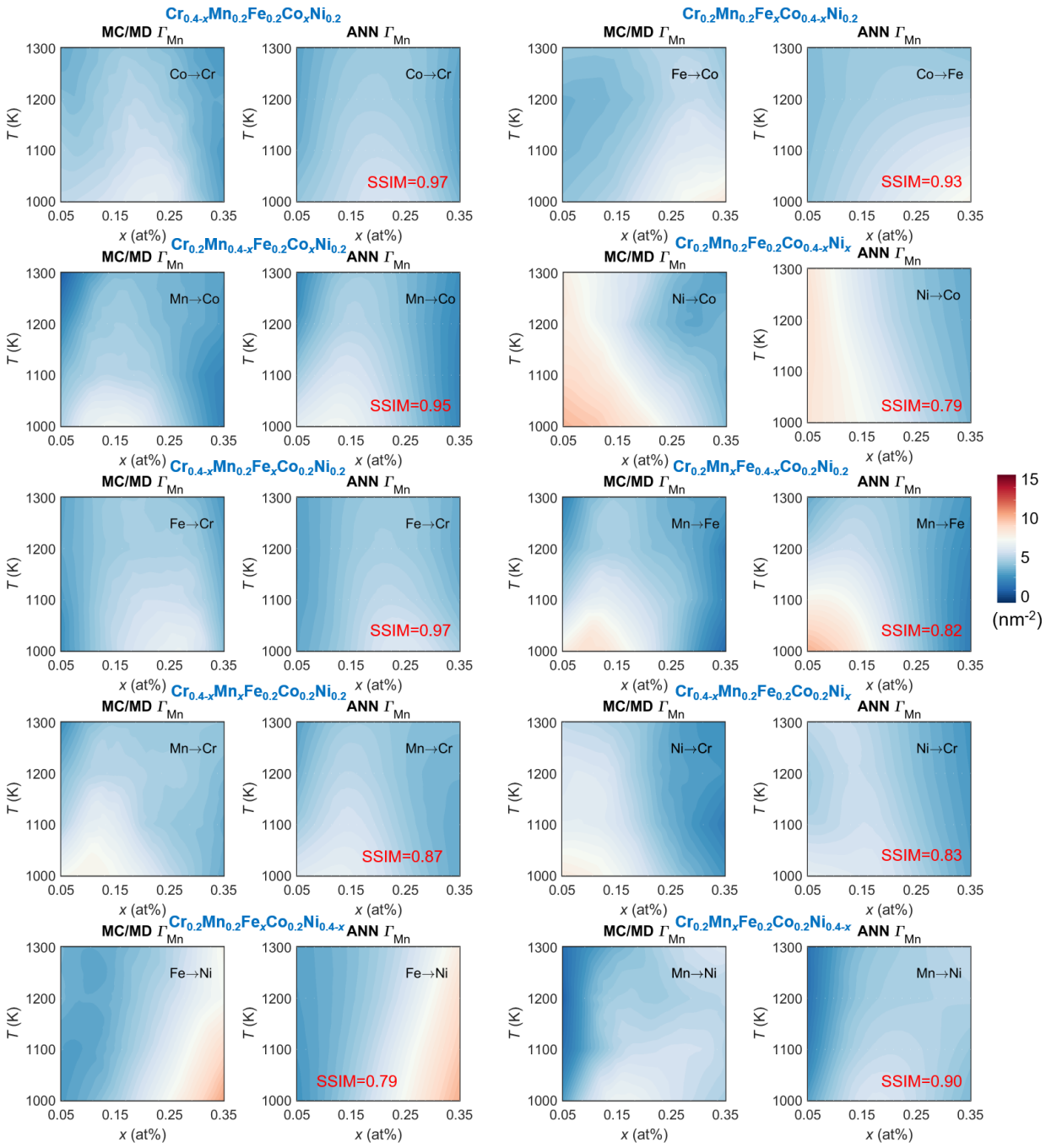

Fig. S20. 10 pairs of ANN-predicted *vs*. hybrid MC/MD-simulated diagrams of GB excess of Mn (Γ_{Mn}). The label of "Co→Ni" indicates that the bulk Co fraction increases from x = 0.05 to 0.35 at%, while replacing Ni (the bulk Ni fraction = $0.4 - x$).

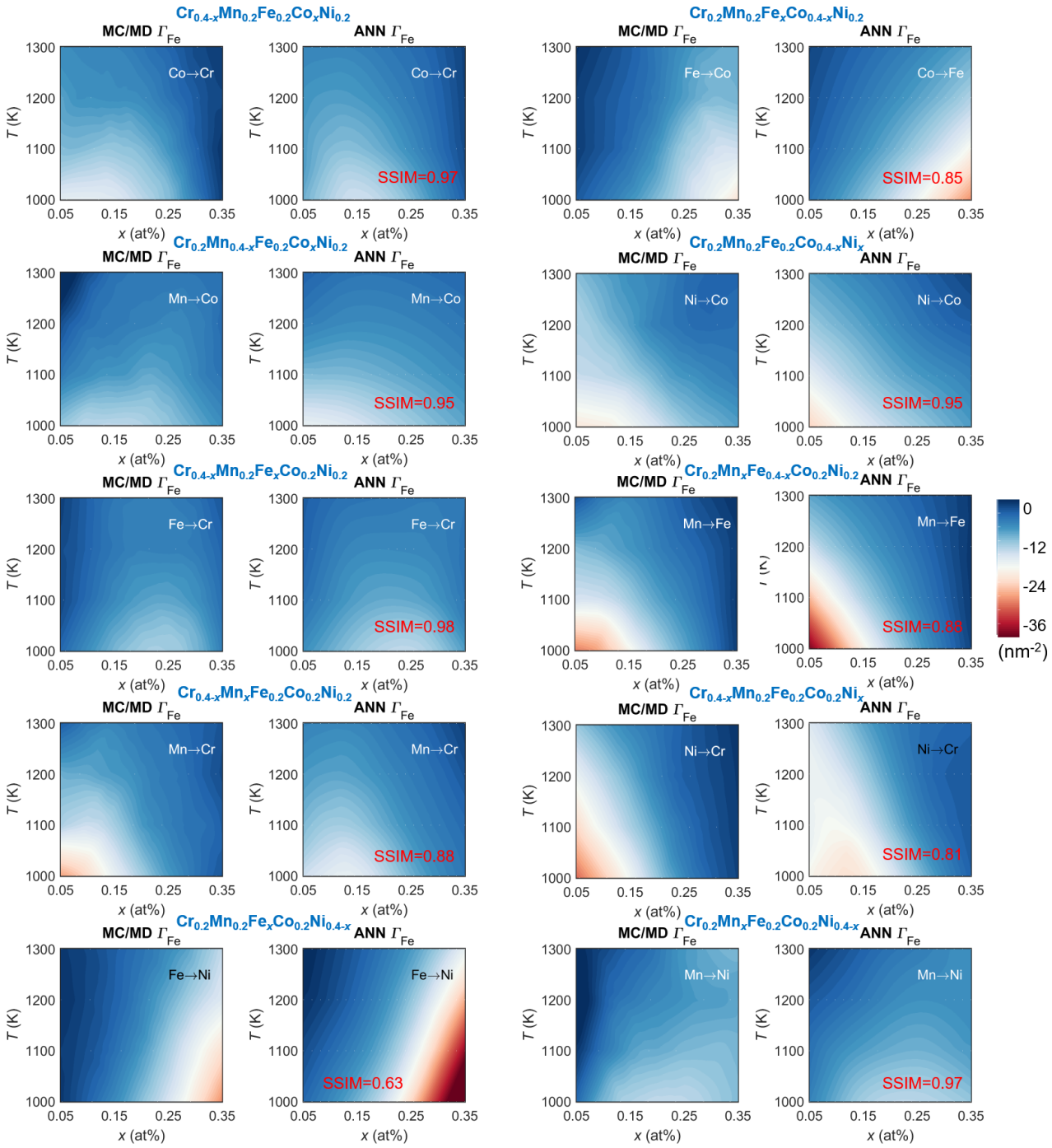

Fig. S21. 10 pairs of ANN-predicted *vs*. hybrid MC/MD-simulated diagrams of GB excess of Fe (Γ_{Fe}). The label of "Co→Ni" indicates that the bulk Co fraction increases from x = 0.05 to 0.35 at%, while replacing Ni (the bulk Ni fraction = $0.4 - x$).

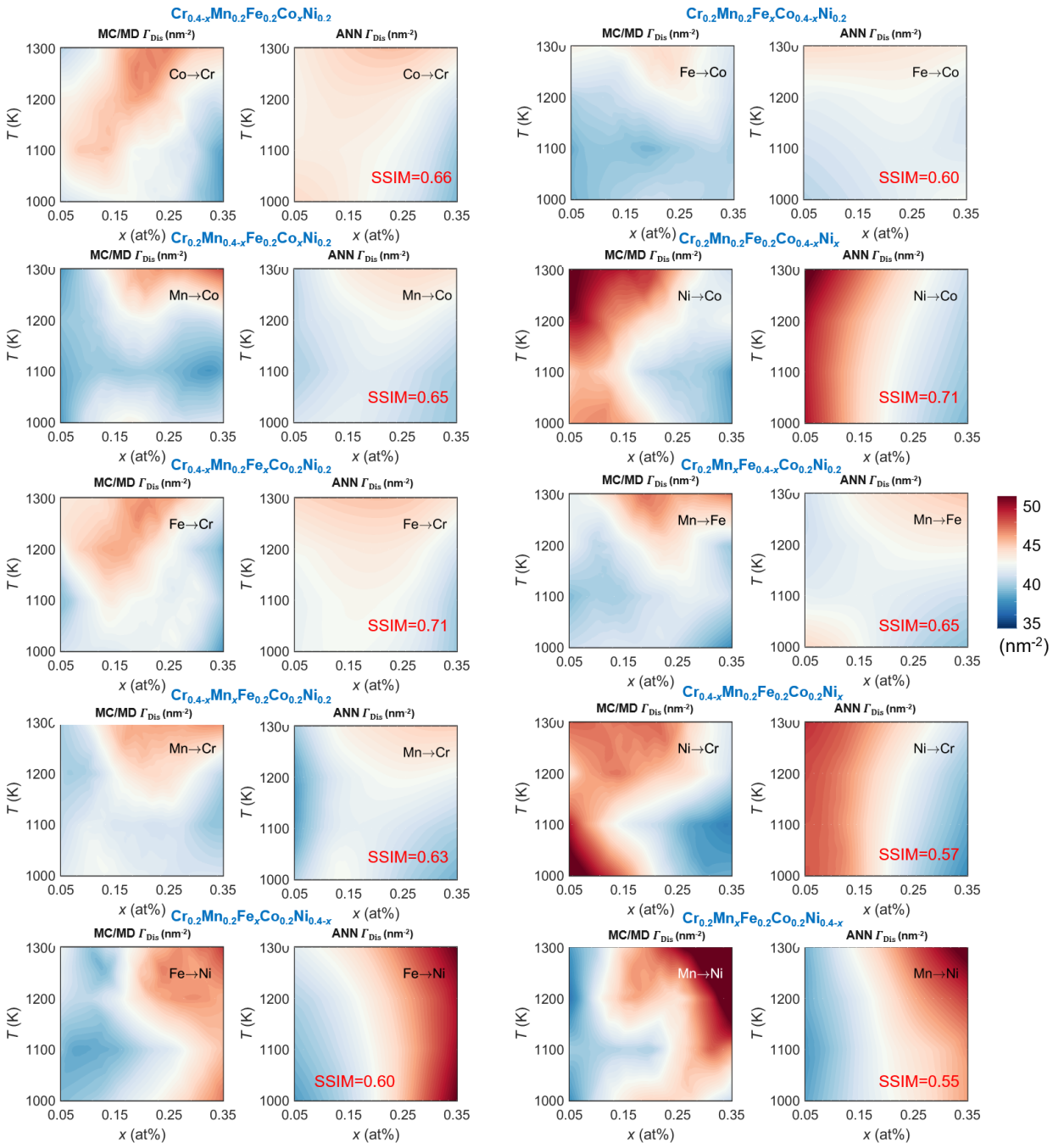

Fig. S22. 10 pairs of ANN-predicted *vs*. hybrid MC/MD-simulated diagrams of GB excess of disorder (Γ_{Dis}). The label of "Co→Ni" indicates that the bulk Co fraction increases from x = 0.05 to 0.35 at%, while replacing Ni (the bulk Ni fraction = 0.4 − x).

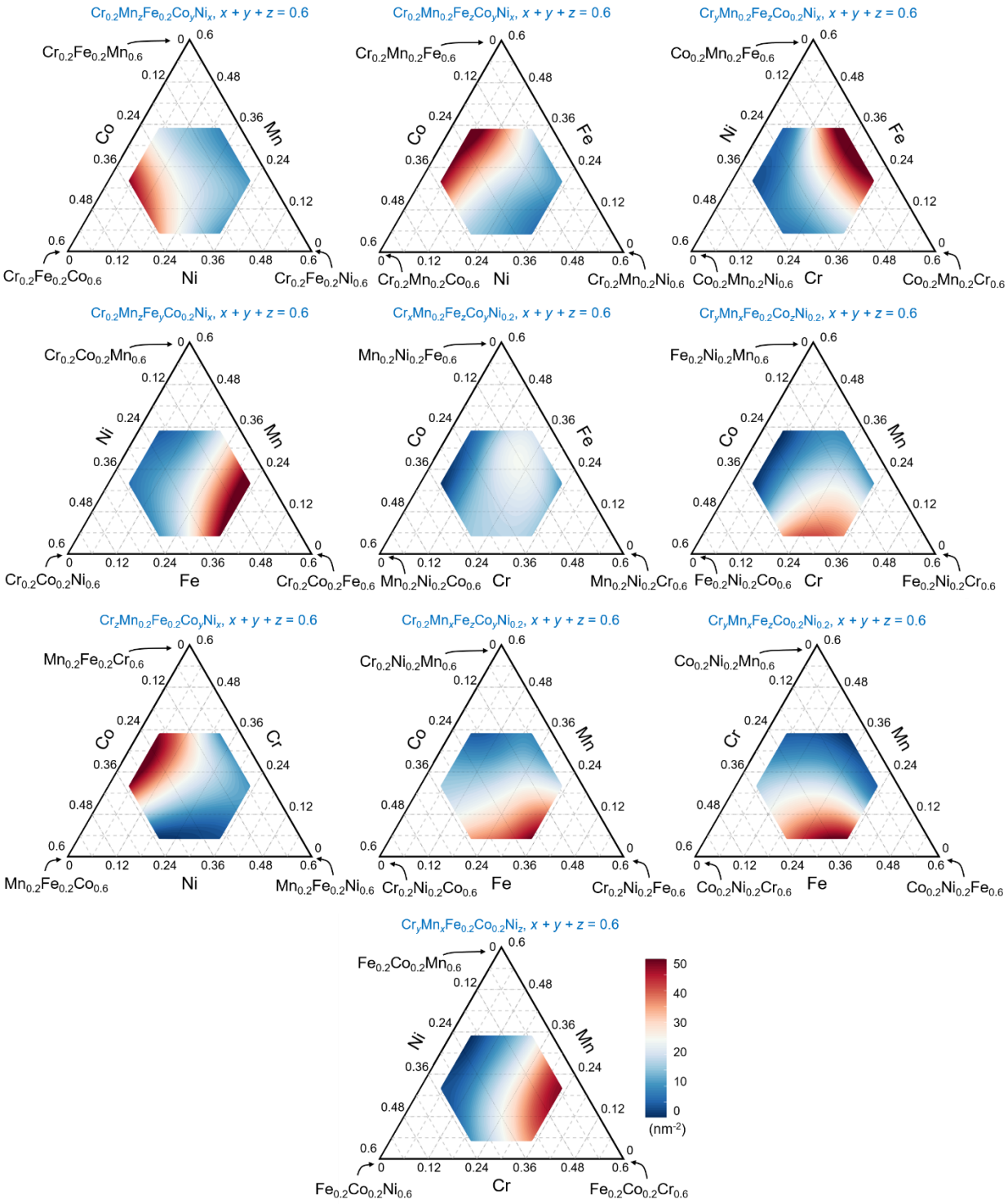

Fig. S23. ANN-predicted ternary diagrams of GB excess of Cr (Γ_{Cr}) for ten different subsystems at 1000 K.

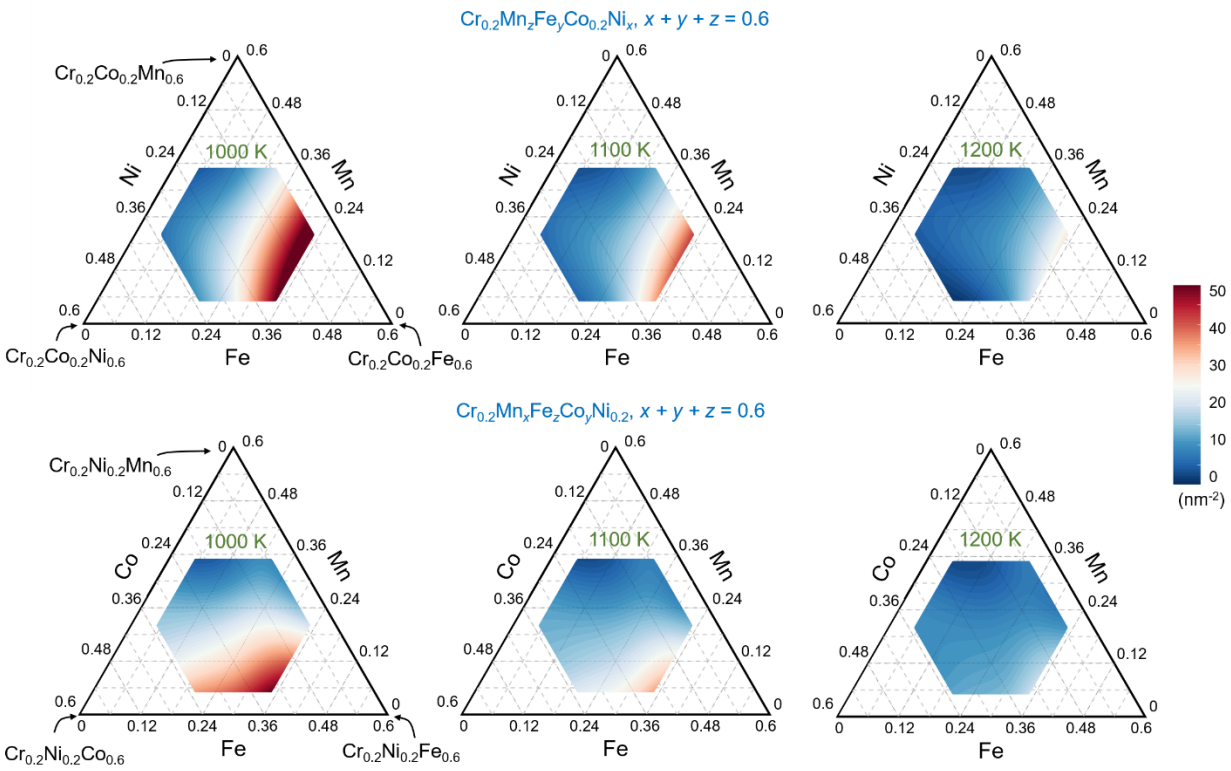

Fig. S24. ANN-predicted ternary diagrams of GB excess of Cr (Γ_{Cr}) for two representative subsystems ($Cr_{0.2}Mn_zFe_yCo_{0.2}Ni_x$ and $Cr_{0.2}Mn_xFe_zCo_yNi_{0.2}$, where $x + y + z = 0.6$) from 1000 K to 1200 K.

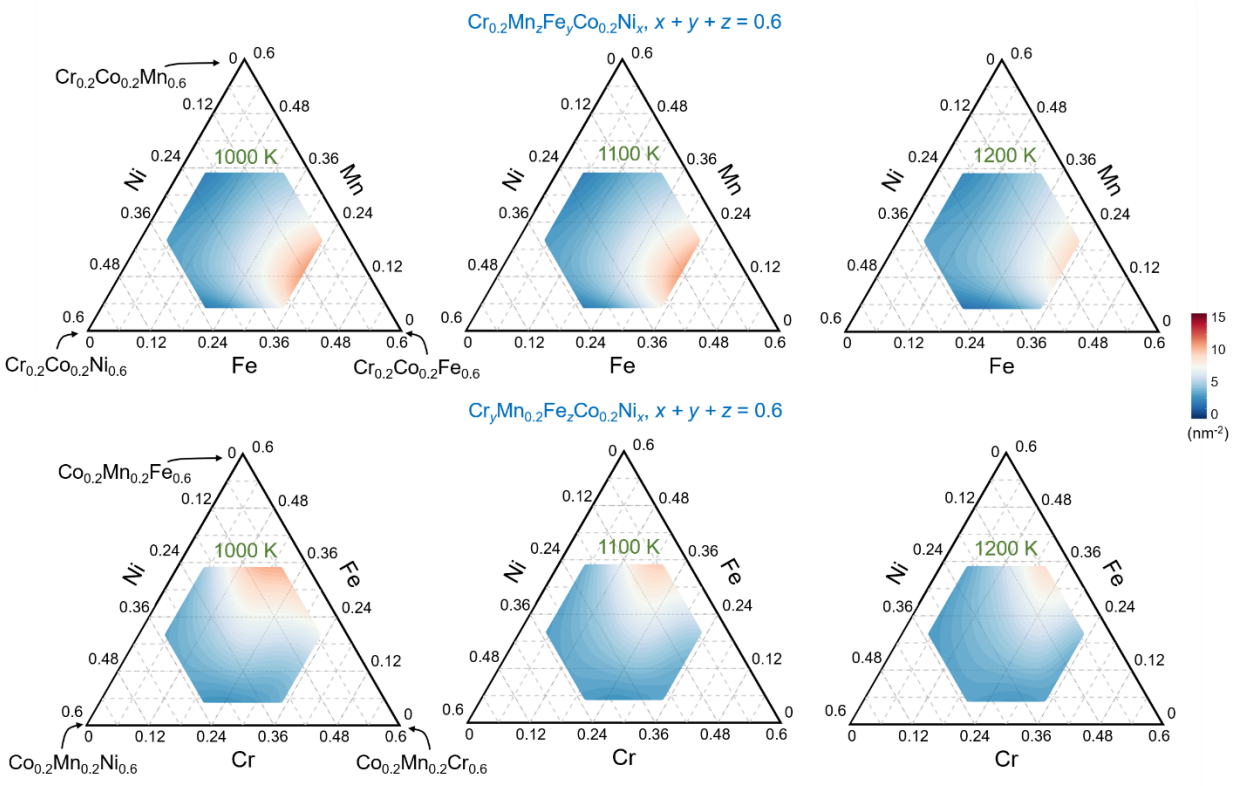

Fig. S25. ANN-predicted ternary diagrams of GB excess of Mn (Γ_{Mn}) for two representative subsystems ($Cr_{0.2}Mn_zFe_yCo_{0.2}Ni_x$ and $Cr_yMn_{0.2}Fe_zCo_{0.2}Ni_x$, where $x + y + z = 0.6$) from 1000 K to 1200 K.

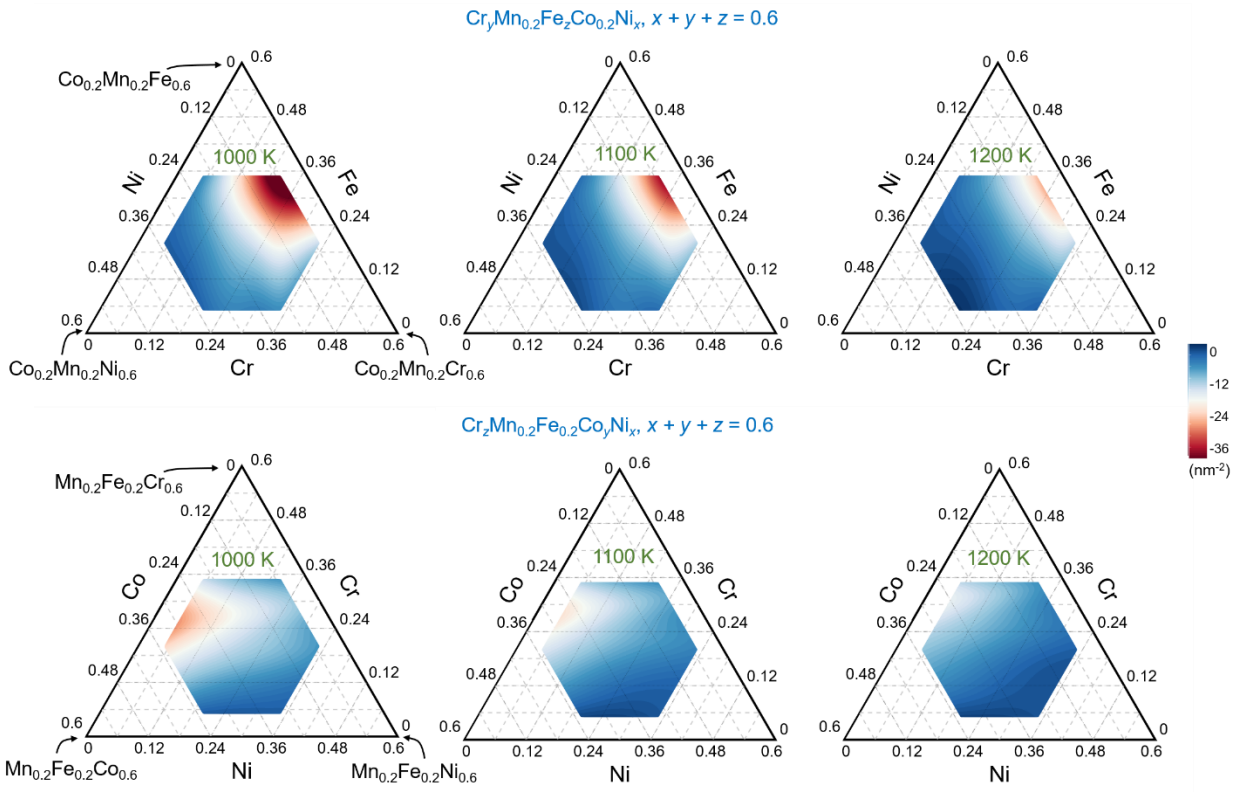

Fig. S26. ANN-predicted ternary diagrams of GB excess of Fe (Γ_{Fe}) for two representative subsystems ($Cr_yMn_{0.2}Fe_zCo_{0.2}Ni_x$ and $Cr_zMn_{0.2}Fe_{0.2}Co_yNi_x$, where $x + y + z = 0.6$) from 1000 K to 1200 K.

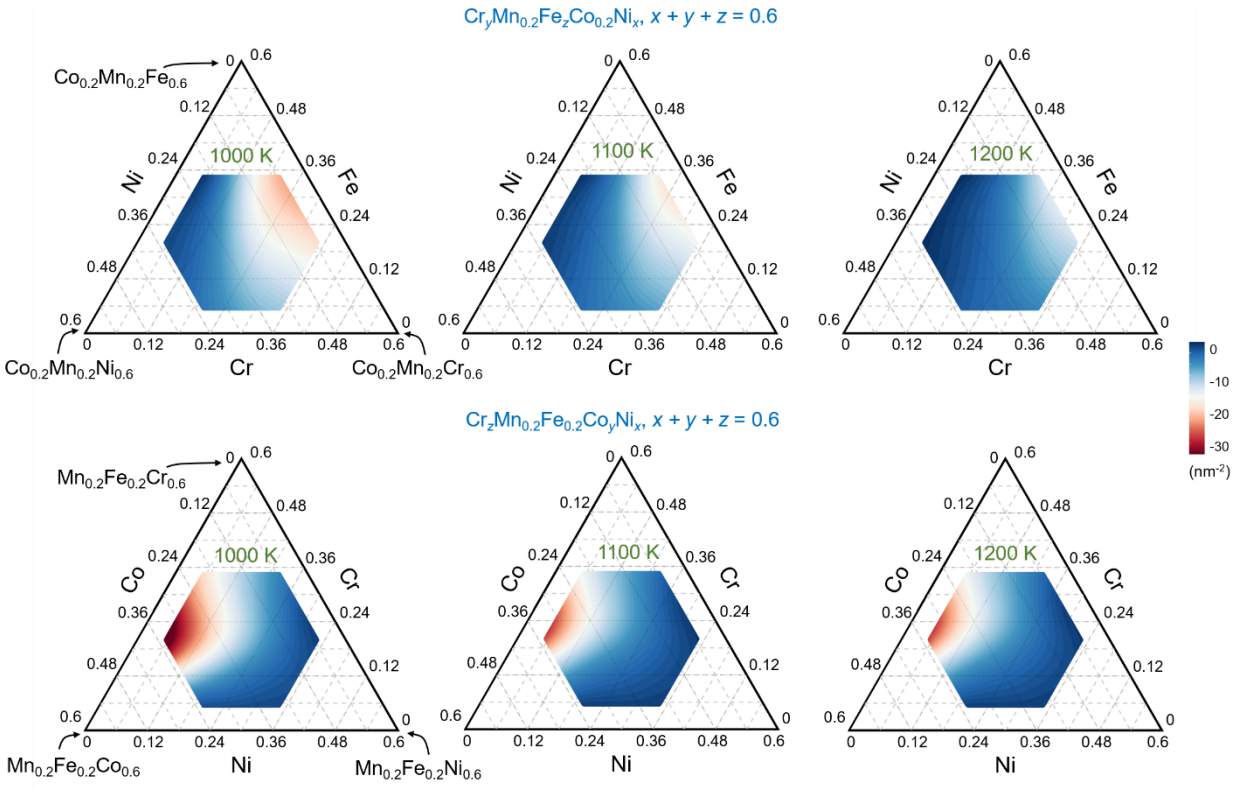

Fig. S27. ANN-predicted ternary diagrams of GB excess of Co (Γ_{Co}) for two representative subsystems (Cr$_y$Mn$_{0.2}$Fe$_z$Co$_{0.2}$Ni$_x$ and Cr$_z$Mn$_{0.2}$Fe$_{0.2}$Co$_y$Ni$_x$, where $x + y + z = 0.6$) from 1000 K to 1200 K.

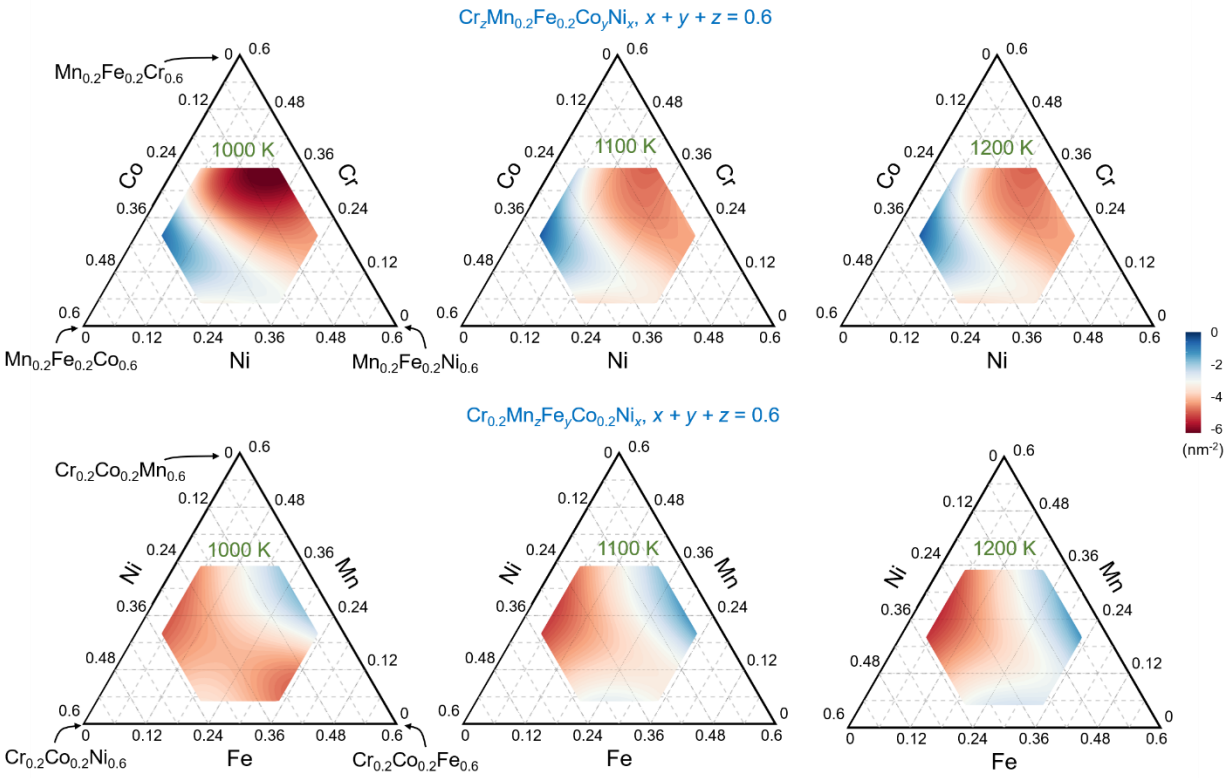

Fig. S28. ANN-predicted ternary diagrams of GB excess of Ni (Γ_{Ni}) for two representative subsystems (Cr$_z$Mn$_{0.2}$Fe$_{0.2}$Co$_y$Ni$_x$ and Cr$_{0.2}$Mn$_z$Fe$_y$Co$_{0.2}$Ni$_x$, where $x + y + z = 0.6$) from 1000 K to 1200 K.

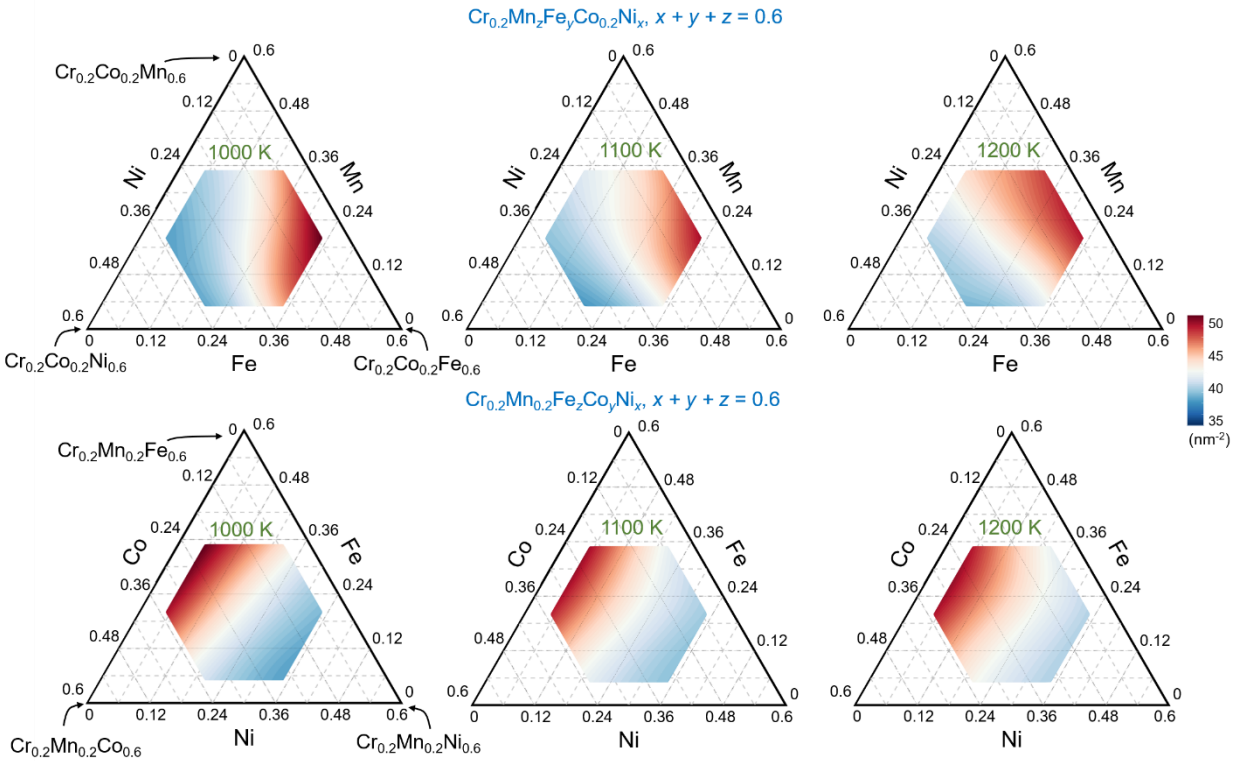

Fig. S29. ANN-predicted ternary diagrams of GB excess of disorder (Γ_{Dis}) for two representative subsystems ($Cr_{0.2}Mn_zFe_yCo_{0.2}Ni_x$ and $Cr_{0.2}Mn_{0.2}Fe_zCo_yNi_x$, where $x + y + z = 0.6$) from 1000 K to 1200 K.

Supplementary References:

1. P. Wynblatt and D. Chatain, *Physical Review Materials*, 2019, **3**, 054004.
2. L. Li, Z. Li, A. Kwiatkowski da Silva, Z. Peng, H. Zhao, B. Gault and D. Raabe, *Acta Materialia*, 2019, **178**, 1-9.
3. K. Ming, L. Li, Z. Li, X. Bi and J. Wang, *Science Advances*, 2019, **5**, eaay0639.
4. P. M. Larsen, S. Schmidt and J. Schiøtz, *Modelling and Simulation in Materials Science and Engineering*, 2016, **24**, 055007.
5. P. Wynblatt and D. Chatain, *Metallurgical and Materials Transactions a-Physical Metallurgy and Materials Science*, 2006, **37A**, 2595-2620.
6. R. H. Fowler and E. A. Guggenheim, *Cambridge university press*, 1939.
7. P. Wynblatt and R. C. Ku, *Surface Science*, 1977, **65**, 511-531.
8. J. Friedel, *Advances in Physics*, 1954, **3**, 446-507.
9. W. Xing, A. R. Kalidindi, D. Amram and C. A. Schuh, *Acta Materialia*, 2018, **161**, 285-294.
10. H. A. Murdoch and C. A. Schuh, *Journal of Materials Research*, 2013, **28**, 2154-2163.
11. D. M. M. Guttmann, *in: W.C. Johnson, J.M. Blakely (Eds.), Interfacial Segregation, Metals Park, ASM, 1979.*, 1979.
12. J. Du Plessis and G. Van Wyk, *Journal of Physics and Chemistry of Solids*, 1988, **49**, 1441-1450.
13. P. Lejček and S. Hofmann, *Journal of Materials Science*, 2021, **56**, 7464-7473.
14. L. Li, R. D. Kamachali, Z. Li and Z. Zhang, *Physical Review Materials*, 2020, **4**, 053603.
15. T. A. Manz, *RSC Advances*, 2017, **7**, 45552-45581.
16. S. Chen, Z. H. Aitken, S. Pattamatta, Z. Wu, Z. G. Yu, R. Banerjee, D. J. Srolovitz, P. K. Liaw and Y.-W. Zhang, *Acta Materialia*, 2021, **206**, 116638.
17. L. Liu and Q.-X. Guo, *Chemical Reviews*, 2001, **101**, 673-696.
18. P. Lejček, S. Hofmann, M. Všianská and M. Šob, *Acta Materialia*, 2021, **206**, 116597.